# Stability of non-Boussinesq convection via the complex Ginzburg-Landau model

Sergey A. Suslov [1,2]

*Department of Mathematics and Computing, University of Southern Queensland, Toowoomba, Queensland 4350, Australia*

Samuel Paolucci

*Aerospace & Mechanical Engineering and Center for Applied Mathematics, University of Notre Dame, Notre Dame, Indiana 46556, U.S.A.*

**Abstract**

A cubic complex Ginzburg-Landau model is derived for the flow of a general fluid near a bifurcation point. Solutions are obtained for the natural convection flow of air in a differentially-heated tall closed cavity under non-Boussinesq conditions. The model is used to analyse various types of instabilities. In particular, it is found that nonlinear fluid properties variations with temperature lead to a convective instability of the flow when the temperature difference becomes sufficiently large. This is in contrast to classical results in the Boussinesq limit where the instability is found to be always absolute. The results obtained using the model for an infinitely tall cavity are in excellent agreement with those of direct numerical simulations for a cavity of aspect ratio 40.

*Key words:* non-Boussinesq convection, weakly nonlinear stability theory, Ginzburg-Landau model
*PACS:* 44.05.+e, 44.25.+f, 47.15.Fe, 47.15.Rq, 47.20.Bp, 47.20.Ft, 47.20.Ky

[1] Corresponding author. Phone: +61-7-4631-5542, Fax: +61-7-4631-5550, E-mail: ssuslov@usq.edu.au

[2] The work of this author was partially supported by an Early Career Researcher Grant from the University of Southern Queensland (2000) and by a computing grant from the Australian Partnership for Advanced Computing (2000).

## 1 Introduction

When properties of a fluid are allowed to vary with temperature and pressure, the momentum and energy equations which describe the flow of a fluid, become substantially more complicated due to the additional nonlinearities arising from density, viscosity, thermal conductivity, and specific heat variations. In the Boussinesq limit, where fluid properties are constant, the governing equations have a quadratic nonlinearity. However, in non-Boussinesq regimes the nonlinearity of the governing equations is largely determined by the form of the constitutive equations and the equation of state for the fluid, and in general it is not even of polynomial character. This is the case, for example, when the well known Sutherland formulae are used to describe viscosity and thermal conductivity.

The nonlinearities associated with fluid property variations play a symmetry-breaking role. In a differentially-heated tall vertical cavity they distort the stationary cubic velocity profile and linear temperature distribution across the cavity which exist in the Boussinesq limit of very small temperature differences (e.g. Rudakov, 1967; Bergholtz, 1978; Lee and Korpela, 1983). This deviation from the symmetric case starts playing an important role in defining the stability characteristics of the flow when the temperature difference between the walls is only about 10% of the average temperature in the cavity (Suslov and Paolucci, 1995b). One consequence is that the parallel basic flow becomes more stable: the critical Grashof number at which it bifurcates to a spatially periodic one increases rapidly. Although the instability leading to transverse rolls is still due to the shear of the flow and first appears near the inflection point of the basic velocity profile, the disturbances are not stationary anymore, in contrast to the Boussinesq limit, and the resulting convection rolls drift downward. In weakly non-Boussinesq convection in a tall vertical cavity, this drift has been detected experimentally, for example, by Simpkins (1989). He observed a slow downward motion of convection rolls in a cavity of aspect ratio 40 for $\epsilon \approx 0.15$ and $Gr \approx 8732$. The speed and cell wavelength of the moving rolls (Simpkins, 1993) were found to be in close agreement with values predicted by two-dimensional linear stability theory (Suslov and Paolucci, 1995b). At very large values of temperature differences between the walls the nonlinear density variation leads to the appearance of a new physical instability driven by buoyancy. The corresponding critical Grashof number decreases rapidly with increasing temperature difference between the walls. This instability appears near the cold wall and the associated disturbances propagate downward much faster than those associated with shear.

The weakly nonlinear hydrodynamic stability theory first suggested by Stuart (1960), Watson (1960), and Stuart and Stewartson (1971), and their modifications by Reynolds and Potter (1967), Sen and Venkateswarlu (1983), and

Herbert (1983), have been shown to be very powerful tools for the stability analysis of various flows. In our earlier work (Suslov and Paolucci, 1997b) we extended the application of Watson's theory to the stability of the flow of a general fluid. The form of the expansion was derived based on the Taylor expansions of properties about the reference distributions. This enabled us to examine successfully the near critical weakly nonlinear states in the differentially-heated cavity problem. In particular, it was confirmed that the shear driven (inflection point) instability is supercritical in the Boussinesq limit, but it was shown to become subcritical at larger values of temperature difference between the walls. The buoyancy driven instability was shown to remain supercritical. At a certain value of temperature difference both instability modes bifurcate simultaneously (the so-called codimension-2 point). The dynamics of the flow in this regime has been explored in Suslov and Paolucci (1997a). It has been shown that the subcritical shear mode triggered by the supercritical buoyancy mode normally dominates the asymptotic behaviour of the flow.

Since both instability modes have a preferred propagation direction under non-Boussinesq conditions, the issue of absolute and convective instabilities arises. When applied to finite size geometries, such as enclosures, these concepts are closely related to the existence of so-called global modes (Pier and Huerre, 1996; Priede and Gerberth, 1997). Their spatial shape is non-trivially influenced in absolutely unstable regimes by the type of boundary conditions which are specified for the model (e.g. Büchel, Lücke, Roth, and Schmitz, 1996). The study by Cross and Kuo (1992) shows that in systems with $y \to -y$ symmetry, which can support counter-propagating waves, a self-sustained disturbance pattern may exist near the ends of an enclosure even in convectively unstable regimes due to the disturbance reflections from boundaries. This is observed, for example, in binary fluid convection in a horizontal layer considered by the above authors. In our study the $y \to -y$ symmetry is broken by the fixed downward direction of the gravity in conjunction with non-Boussinesq fluid property variations. As a result the disturbances are found to propagate only downwards in the considered non-Boussinesq regimes (they have negative group and phase speeds in contrast to the Boussinesq limit where the disturbances have zero group and phase speeds). As noted, for example, by Aranson and Kramer (2002), in such a situation detailed consideration of wave reflections can be avoided and thus leading to a significant simplification of the analysis. First, this is because there are no waves incident to the upper wall to be reflected. Second, the disturbances reflected from the bottom wall cannot propagate far back into the flow domain. Indeed the group speed of the reflected disturbances is still negative and they can only diffuse back. Their diffusion speed is normally much slower than the propagation group speed. Therefore the reflected disturbances are swept back to the wall where the energy loss due to its absorbing nature kills the reflected disturbances before they can be felt far back in the flow domain, unless the flow is absolutely unstable.

But even in this case the global influence of the boundaries is due to diffusion and not to the wave reflections. Such influence is much easier to account for as it depends mostly on the properties of the model equation valid in the "bulk" of the fluid rather than on the specific (unknown) reflection coefficients of the walls. Because of these arguments the spatio-temporal instability character remains very similar to that of open flows and the influence of the top and bottom wall boundary conditions on the model solutions is found to be weak. In practice imposing intuitive zero boundary conditions for the disturbance amplitudes, governed by the derived Ginzburg-Landau equations, results in solutions that sufficiently far away from the top and bottom walls are found to be in excellent qualitative and quantitative agreement with those from *d*irect *n*umerical *s*imulations (DNS) of the full equations with the appropriate physical boundary conditions. This agreement motivated us to undertake the following simplified approach. Effectively, for analysis purposes, we consider an infinitely tall enclosure with no detailed treatment of the top and bottom boundaries. The fact that the cavity is closed enters only in the context of global fluid mass conservation at the disturbance development stage which results in a non-trivial constraint when fluid density is allowed to vary. We only mimic the physical boundary conditions when comparisons with DNS results are made. Such an approach is also justified by the fact that a parallel basic flow, which is the starting point for the derivation of the reduced amplitude models, does not exist near the top and bottom ends so that it does not make much sense to study the detailed influence of the boundary conditions onto the model behaviour in the regions where the model itself becomes irrelevant. Any such detail would be completely obscured by the effects of nonparallel turning flow which is virtually impossible to describe using weakly nonlinear arguments.

Having explained such simplified treatment, in this work we focus on the influence of the non-Boussinesq fluid properties variations on the spatio-temporal evolution of the "bulk" solutions (sufficiently far from the ends) to the natural convection problem. The present work provides a general theoretical framework based on a weakly spatial modulation approach to analyse the character of instabilities in non-Boussinesq convection.

Spatio-temporal instabilities of various fluid flows have been the subject of many studies in the last decade. Recent works reported by Brevdo (1995), Lingwood (1997), Carrière and Monkewitz (1999), Moresco and Healey (2000), and references therein, are just few such examples. In brief, these studies deal with the analysis of disturbances which can grow in space and time. If the disturbance grows at any spatial location, such instability is referred to as absolute while if the asymptotically growing disturbance is observed only in a moving system of coordinates, but not in a stationary one, the situation is referred to as convective instability. The strict mathematical formalism of determining the character of an instability in a problem is accomplished

through analysis of the dispersion relation over a complex wavenumber space (see Huerre and Monkewitz, 1985, 1990; Brevdo, 1988). This approach, although accurate, has two obvious disadvantages. First, analysing the topography of multiple branches of a physical dispersion relation in the complex space, while straightforward and informative for a simple relation, is an expensive and technically involved numerical task for a non-trivial one. Second, this approach is linear in nature and therefore cannot predict characteristics of saturated supercritical states. For these reasons the idea of reducing the full physical problem to a simpler weakly nonlinear model and analysing it, instead of the original problem, is very appealing (see, for example, Suslov, 1997; Büchel and Lücke, 2000).

The simplest mathematical model which describes convective and absolute instability scenarios for a (small) disturbance amplitude $A$ is the complex Ginzburg-Landau equation (CGLE)

$$\frac{\partial A}{\partial t} + c_g \frac{\partial A}{\partial y} = \sigma A + K_2 \frac{\partial^2 A}{\partial y^2} + K_1 A |A|^2 . \tag{1}$$

This model has been the subject of extensive studies, and many of its solutions, including fully nonlinear, have been obtained, well understood and catalogued (e.g. Newell, 1974; Nozaki and Bekki, 1983, 1984; Landman, 1987; Cross and Hohenberg, 1993; Tobias et al., 1998; Huerre, 2000; Aranson and Kramer, 2002), making the use of this model for analysing complicated physical flows even more appealing. However, the major criticism of such an approach is that it is generally difficult to prove the relevance of the CGLE to the original full problem. This difficulty is two-fold: the mathematical form of (1) has to be justified and, subsequently, its actual coefficients have to be chosen to reflect accurately the properties of the original full problem. In the literature, an abstract CGLE is frequently analysed without relating the quantitative results to any specific physical problem in a consistent manner. The danger of this is noted, for example, by Carrière and Monkewitz (1999). It was shown there that discrepancy exists between the accurate convective/absolute instability results based on the saddle point analysis of the dispersion relation and results based on the Ginzburg-Landau model for convection in a horizontal fluid layer with through-flow (Müller et al., 1993). In the present work special care is taken to guarantee that the derived CGLE remains a relevant and quantitatively accurate model for the complete range of parameters describing the physical problem of non-Boussinesq convection in the differentially-heated tall vertical cavity.

The concepts of convective and absolute instabilities originally based on the properties of the linearised dispersion relation (Huerre and Monkewitz, 1990) have been generalised to incorporate finite amplitude perturbations, (see Chomaz, 1992) where the concepts of nonlinear convective and absolute instabilities were introduced. The idea behind them is to trace the dynamics of propa-

gating fronts separating the regions with finite disturbances from undisturbed ones. The boundary of nonlinear absolute instability was found to coincide with that of linear absolute instability in such flows as wakes (Delbende and Chomaz, 1998), Taylor-Couette flow (Büchel et al., 1996) and Rayleigh-Bénard convection (Fineberg and Steinberg, 1997). This conclusion was made based on either relatively expensive numerical simulations of the full flow equations or experiments. Couairon and Chomaz (1997) show that if the flow can be modelled by the supercritical cubic Ginzburg-Landau equation this should always be the case. In contrast, if the corresponding model is a subcritical quintic GLE then the nonlinear absolute instability may occur even in linearly stable regimes. The numerical simulations that we report in Section 5 indeed indicate that this can be the case in non-Boussinesq natural convection. This emphasises once again the important role which the properly derived CGLE can play in the analysis of flow instabilities and resulting flow patterns.

Another aspect deserving attention is the character of the coefficients entering (1). The CGLE model has been studied extensively and its derivation is thought to be common knowledge. Details of such derivations for any particular physical problem are normally lengthy and are rarely reported in the literature in full (see, for example, Büchel and Lücke, 2000). Nevertheless, here we endeavour to provide a fully consistent derivation for a fairly general two-dimensional flow. The major purpose of this exercise is to develop a reliable criterion for the accuracy of the cubic Ginzburg-Landau model. In particular, we will show that if the physical dispersion relation deviates from quadratic over the wavenumber range corresponding to the positive linear amplification rates, then the linearised Ginzburg-Landau model cannot be used to accurately determine the character of spatio-temporal instabilities arising in a problem. This explains, for example, why the range of validity of the Ginzburg-Landau equation modelling binary fluid convection becomes smaller with increasing Reynolds number of a through-flow (Büchel and Lücke, 2000).

In this paper the problem of non-Boussinesq natural convection of a fluid with realistic property variations in a two-dimensional differentially-heated tall vertical cavity is formulated in Section 2. The Appendices A-D contain a detailed derivation of a general CGL model using the approach previously suggested by the authors (Suslov and Paolucci, 1997b). This approach uses the appropriate orthogonality conditions along with the conventional solvability conditions which extend the applicability region further away from a marginal stability surface. The major goal of Section 4 is to suggest a simple and computationally inexpensive quantitative accuracy test and a method for error bound estimation for the developed CGL model. This becomes possible by following a somewhat untraditional discussion of the CGLE with coefficients evaluated at a wavenumber different from that providing the maximum amplification rate. A careful physical interpretation of such an equation and its solutions is given in Section 3. Once the developed accuracy test is shown to

be satisfied in all regimes of interest, the wide range of physical results for non-Boussinesq natural convection in a tall cavity are obtained and reported in Section 5. Special attention is given to quantitative comparisons of the model results for an effectively infinitely tall cavity and DNS results of a flow in a cavity of large but finite aspect ratio. To account for the interaction of two instability modes in the strongly non-Boussinesq regimes, the globally coupled equations, derived in Appendix E, are solved numerically. The major findings of the present study are summarised in Section 6.

## 2 Problem definition

We consider the two-dimensional convection flow in a tall rectangular air-filled cavity of width $H$ with isothermal vertical walls maintained at the different temperatures $T_h^*$ and $T_c^*$ respectively (asterisks denote dimensional quantities). A uniform downward gravitational field of magnitude $g$ is parallel to the vertical walls. In the case of large temperature differences $\Delta T = T_h^* - T_c^* > 0$ the flow is described by the dimensionless low-Mach-number equations (Paolucci, 1982; Chenoweth and Paolucci, 1986):

$$\rho\left(\frac{\partial u_i}{\partial t} + u_j\frac{\partial u_i}{\partial x_j}\right) = -\frac{\partial \Pi}{\partial x_i} + \frac{\mathrm{Gr}}{2\epsilon}(\rho - 1)n_i + \frac{\partial \tau_{ij}}{\partial x_j}\,, \tag{2}$$

$$\rho\left(\frac{\partial T}{\partial t} + u_j\frac{\partial T}{\partial x_j}\right) = \Gamma\beta T\frac{\mathrm{d}P}{\mathrm{d}t} + \frac{1}{\mathrm{Pr}}\frac{\partial}{\partial x_j}\left(k\frac{\partial T}{\partial x_j}\right)\,, \tag{3}$$

$$\frac{\partial \rho}{\partial t} + \frac{\partial \rho u_j}{\partial x_j} = 0\,, \tag{4}$$

where

$$\tau_{ij} = \mu\left[\left(\frac{\partial u_i}{\partial x_j} + \frac{\partial u_j}{\partial x_i}\right) - \frac{2}{3}\delta_{ij}\frac{\partial u_k}{\partial x_k}\right]\,. \tag{5}$$

As shown by Paolucci (1982), in the low-Mach-number expansions which result in the above equations, the total pressure decomposes into the spatially uniform thermodynamic component $P = P(t)$ and the dynamic/hydrostatic component $\Pi = \Pi(x_i, t)$. In writing (5), Stokes' hypothesis is used to relate the coefficient of bulk viscosity to the dynamic viscosity. Here $u_i = (u, v)$ and $x_i = (x, y)$ are velocity components and coordinates in the horizontal and vertical directions respectively and $n_i = (0, -1)$ is the unit vector in the direction of gravity. The equations are made dimensionless by using the enclosure width $H$, the reference temperature $T_r = \left(T_h^* + T_c^*\right)/2$, the viscous speed $u_r = \mu_r/(\rho_r H)$, the characteristic time $t_r = H/u_r$, the initial thermodynamic pressure $P_r$ which would exist in the cavity with a stationary fluid at the reference temperature, and the characteristic value of the dynamic pressure

$\Pi_r = \rho_r u_r^2$. All properties of the fluid are non-dimensionalised by using their respective values evaluated at the reference temperature and thermodynamic pressure.

The above system is complemented by the non-dimensional equation of state relating the fluid density $\rho$, the temperature $T$ and the spatially uniform thermodynamic pressure $P$. While the procedure developed in this work is absolutely general, all specific numerical results are given for air as the working fluid so that the appropriate equation of state is that of an ideal gas (Paolucci, 1982)

$$\rho = \frac{P}{T}\,, \tag{6}$$

constant specific heat at constant pressure,

$$c_p = 1\,, \tag{7}$$

and constitutive equations for the transport properties, namely the Sutherland laws for dynamic viscosity $\mu$ and thermal conductivity $k$

$$\mu = T^{3/2}\left(\frac{1+S_\mu}{T+S_\mu}\right)\,, \quad k = T^{3/2}\left(\frac{1+S_k}{T+S_k}\right)\,, \tag{8}$$

where, according to White (1974), $S_\mu = S_\mu^*/T_r = 0.368$ and $S_k = S_k^*/T_r = 0.648$ for $T_r = 300$ K. We also take the Prandtl number $\mathrm{Pr} \equiv \mu_r c_{pr}/k_r = 0.71$, and the fluid resilience parameter $\Gamma \equiv (\gamma_r - 1)/(\gamma_r \sigma_r T_r) = \frac{2}{7}$, corresponding to the ratio of specific heats $\gamma_r \equiv c_{pr}/c_{vr} = \frac{7}{5}$ for an ideal gas since it follows from the equation of state that the coefficient of tension is given by $\sigma \equiv ((\partial P/\partial T)/P)|_\rho = 1/T$. Other parameters are the non-dimensional temperature difference between the walls $\epsilon \equiv \beta_r \Delta T/2$ and the Grashof number $\mathrm{Gr} \equiv \rho_r^2 \beta_r g \Delta T H^3/\mu_r^2$, where $\beta \equiv -\left((\partial\rho/\partial T)/\rho\right)|_P = 1/T$ is the coefficient of volume expansion.

The dimensionless global mass conservation condition

$$\int_V \rho \,\mathrm{d}V = 1\,, \tag{9}$$

where $V$ is the cavity volume, completes the system of equations describing the fluid flow.

The boundary conditions for the problem are

$$u = v = 0 \quad \text{and} \quad T = 1 \pm \epsilon \quad \text{at } x = 0, 1\,. \tag{10}$$

The distant no-penetration boundary conditions at the top and bottom of the closed cavity lead to zero average mass flux through any horizontal cross-section. Allowing for periodicity in the vertical direction with arbitrary wave-

length $\lambda$, this condition can be written as

$$\int_0^1 \left( \frac{1}{\lambda} \int_{y_0}^{y_0+\lambda} \rho v \, \mathrm{d}y \right) \mathrm{d}x = 0 \,, \tag{11}$$

where $y_0$ is an arbitrary vertical location sufficiently far from the ends. This condition leads to the appearance of a uniform vertical pressure gradient whenever the temperature difference between the walls is finite and the flow loses symmetry due to property variations (Suslov and Paolucci, 1997b). This pressure gradient is responsible for the preferred propagation direction of disturbances. Note that although the global conservation conditions (9) and (11) are induced by the distant boundary conditions they do not contain any specific information about the top and bottom ends except that they are closed. These conditions cannot be treated as boundary conditions for the model which will be discussed in the next section. Furthermore, in the Boussinesq limit, conditions (9) and (11) are trivially satisfied since density is treated as constant and the resulting problem is centro-symmetric.

It has been shown by Chenoweth and Paolucci (1985) that for a tall enclosure, a two-dimensional steady parallel basic flow exists over most of the enclosure far enough away from the top and bottom walls. These walls cause the basic flow to reverse. The turning flow existing in the proximity of the top and bottom walls is not parallel and is a natural source of disturbances for the primary parallel flow existing sufficiently far from the ends. The exact form of these disturbances is virtually impossible to establish without solving the full problem. At the same time, if the cavity is sufficiently tall, these details will be shown not to have any significant influence on the bulk flow due to the fact that long-range reflectional influences of the top and bottom walls are not possible in this problem due to the broken reflectional symmetry discussed in the Introduction. Thus only the spatio-temporal evolution of disturbances in the bulk of fluid is investigated in the subsequent sections by means of the Ginzburg-Landau theory and DNS.

## 3 Complex Ginzburg-Landau model

Suslov and Paolucci (1997b) developed an expansion procedure and multiple time scale analysis for the system of equations describing a fluid with general properties. Here we generalise the expansions by allowing multiple spatial scales in the longitudinal coordinate direction in order to account for spatial modulations of the disturbance wave. We assume that a small-amplitude periodic disturbance is superimposed on the fully developed stationary parallel basic flow. Since the most unstable disturbances have been shown to be two-dimensional (Suslov and Paolucci, 1995b), we restrict ourselves to the two-

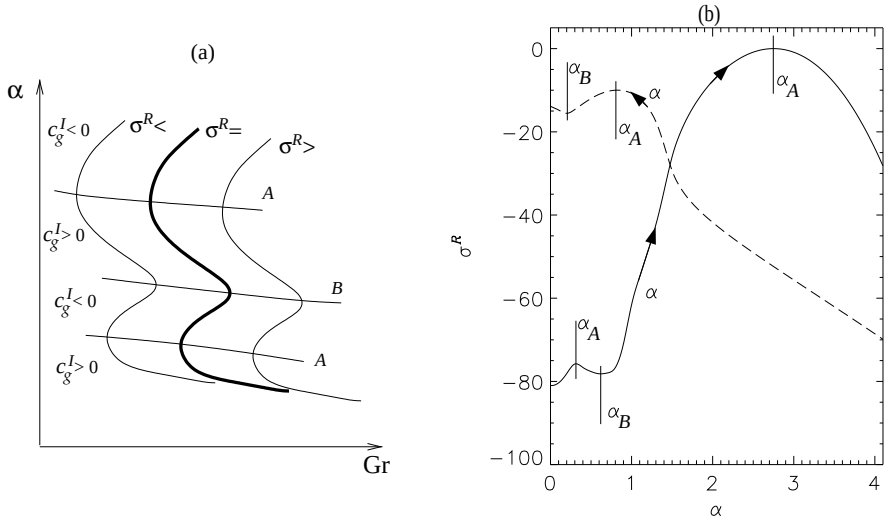


Fig. 1. (a) Sketch of a typical linear stability diagram (thick line): the wave group speed is real only along curves $A$ and $B$. (b) Real parts of the leading eigenvalues for the non-Boussinesq natural convection problem ($\epsilon = 0.3$ and Gr $= 9275$, solid and dashed lines correspond to the shear and buoyancy modes, respectively): the $\sigma^R(\alpha)$ curves have multiple inflection points where $K_2^R$ changes sign.

dimensional case. So as not to detract from the major points of the present work, we have relegated the detailed derivation of (1) to Appendices A–D. Here, for convenience of later discussions, we rewrite the CGLE model in a frame moving with some constant speed $v$ as

$$\frac{\partial A}{\partial t} + (c_g - v)\frac{\partial A}{\partial Y} = \sigma A + K_2 \frac{\partial^2 A}{\partial Y^2} + K_1 A|A|^2 , \tag{12}$$

where $Y = y - vt$, and $c_g$, $K_1(\alpha)$ and $K_2(\alpha)$ are given by (B.8), (D.8) and (D.9), respectively. This model describes the evolution of a spatially modulated monochromatic disturbance wave with wavenumber $\alpha$.

### *3.1 Linearised CGLE: convective and absolute instabilities*

Consider equation (12) linearised about the trivial solution $A = 0$. This corresponds to the linear stability analysis of the basic flow with respect to a weakly modulated spatially periodic wave with fixed wavenumber $\alpha$. Naturally, this is an idealisation since any realistic disturbance is represented by a finite wave envelope rather than by a single sinusoidal wave. Nevertheless, it is instructive to carry out this analysis to obtain some insight into the early stages of the disturbance development. Applying the Fourier transform in $Y$ to the linearised CGLE, and suppressing notations of explicit parametric dependence

on $\alpha$, we obtain

$$\frac{\partial}{\partial t}\bar{A}(t,\beta) = \left[\sigma^R - \mathrm{i}(c_g - v)\beta - K_2\beta^2\right]\bar{A}(t,\beta)\,,$$
$$\bar{A}(0,\beta) = \bar{A}_0(\beta)\,,$$

where $\bar{A}(t,\beta) = \int_{-\infty}^{\infty} A(t,Y)\exp(-\mathrm{i}\beta Y)\,\mathrm{d}Y$. Thus

$$\bar{A}(t,\beta) = \bar{A}_0(\beta)\mathrm{e}^{\left[\sigma^R - \mathrm{i}(c_g - v)\beta - K_2\beta^2\right]t}.$$

Taking the inverse transform we obtain the solution of the linearised CGLE:

$$A(t,Y) = \frac{\mathrm{e}^{\sigma^R t}}{2\sqrt{\pi K_2 t}}\int_{-\infty}^{\infty} A_0(\tilde{y})\mathrm{e}^{-\frac{[Y-(c_g-v)t-\tilde{y}]^2}{4K_2 t}}\,\mathrm{d}\tilde{y}\,. \tag{13}$$

For $K_2^R > 0$ (near $\alpha = \alpha_A$ in Fig. 1(a)), following the definitions given in Deissler (1986), we distinguish three situations: absolute instability, convective instability, and absolute stability of the asymptotic solution $A = 0$. Consider the limit $t \to \infty$ in the coordinate system moving with velocity $v$:

$$A(t\to\infty, y - vt = \text{const.}) \sim \frac{\exp\left[\left(\sigma^R - \frac{(c_g-v)^2}{4K_2}\right)t\right]}{\sqrt{K_2 t}}\,.$$

If

$$\gamma_v \equiv \sigma^R - \frac{\left[\left(c_g^R - v\right)^2 - \left(c_g^I\right)^2\right]K_2^R + 2c_g^I\left(c_g^R - v\right)K_2^I}{4|K_2|^2} > 0\,, \tag{14}$$

then the amplitude grows in this frame. Note that the condition of instability in the stationary ($v = 0$) coordinate system is

$$\gamma_0 \equiv \sigma^R - \frac{\left[\left(c_g^R - v\right)^2 - \left(c_g^I\right)^2\right]K_2^R + 2c_g^I c_g^R K_2^I}{4|K_2|^2} > 0 \tag{15}$$

which corresponds to the case when the disturbance grows with time at any fixed point $y$, i.e. to *absolute instability*. It is easy to show that the extremum of $\gamma_v$ is obtained in a frame moving with speed

$$v_m = c_g^R + c_g^I K_2^I/K_2^R, \tag{16}$$

and the amplification rate in this frame is

$$\gamma_m \equiv \sigma^R + \left(c_g^I\right)^2 / \left(4K_2^R\right)\,. \tag{17}$$

Thus, when $K_2^R > 0$, if

$$d \equiv 4K_2^R\sigma^R + \left(c_g^I\right)^2 > 0, \tag{18}$$

there exists a moving system of coordinates with respect to which the disturbance grows. If at the same time $\gamma_0 < 0$, the amplitude decays at any fixed stationary point. This corresponds to the case of *convective instability*, i.e. the disturbance grows only in the moving frame of reference. The fastest growth rate is observed in the frame moving with velocity given by (16), which is the wave packet propagation speed in a dispersive medium. It is important to note that $d \geq 0$ along the marginal stability surface (thick line in Fig. 1 (a)), meaning that any state which is neutral according to temporal linear stability theory is convectively or absolutely unstable provided $K_2^R > 0$ and $c_g^I \neq 0$. If $d < 0$, the disturbance amplitude decays with respect to the stationary as well as any moving frame of reference. Such a flow is referred to as *absolutely stable*.

Note that if $d > 0$, equating (14) to zero gives an equation for the velocities of the edges of a localised disturbance (the disturbance amplification rate at the edges is equal to zero):

$$v_{1,2} = v_m \pm \sqrt{d}\frac{|K_2|}{K_2^R}\,. \tag{19}$$

It follows that the localised disturbance always spreads with rate

$$\tilde{v} \equiv |v_1 - v_2| = 2\sqrt{d}\frac{|K_2|}{K_2^R} \tag{20}$$

as it develops. In view of (19), the flow is absolutely unstable if $|v_m| < \sqrt{d}|K_2|/K_2^R$.

These types of behaviours are illustrated in Figs. 2 and 3 for the Gaussian initial condition $A_0(y) = a_0 \exp(-ay^2)$ ($a_0$ and $a$ are real positive constants). Solution (13) in a stationary frame ($v = 0$) becomes

$$A(t,y) = \frac{a_0}{\sqrt{1+4aK_2t}} \exp\left[\sigma^R t - a\left(y - c_g t\right)^2\right].$$

When $K_2^R > 0$ (near $\alpha = \alpha_B$ in Fig. 1(a)), cases of absolute stability and convective and absolute instability are distinguished in Fig. 2. We intentionally have chosen $\sigma^R < 0$ to emphasise that the formal solutions of the CGLE can grow even when the sign of the linear growth rate $\sigma^R$ indicates linear stability of a wave with the chosen wavenumber (we interpret this result later in this section). Note that in order for convective instability to occur in such regimes it is necessary, but not sufficient, to have $d > 0$: only sufficiently localised or, equivalently, modulated initial distributions such as that in Fig. 2 (b) can grow convectively when $\sigma^R < 0$. Less localised packets (which are more compact in Fourier space i.e. closer to a monochromatic wave), as shown in Fig. 2 (c), will decay. Thus, in subcritical regimes one should expect a strong dependence

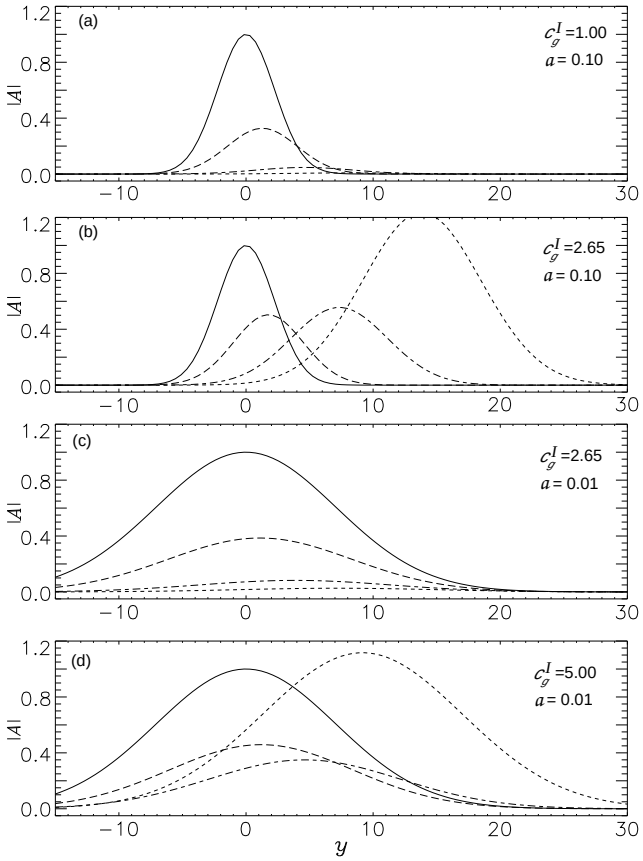


Fig. 2. (a) and (c) Absolutely stable, (b) convectively unstable, and (d) absolutely unstable solutions of the linear CGLE with Gaussian initial condition for $\sigma^R = -1$, $c_g^R = K_2^R = K_2^I = 1$, and $v = 0$: $t = 0$ (solid lines), $t = 1$ (dashed lines), $t = 3$ (dash-dotted lines), and $t = 5$ (dotted lines).

of the asymptotic behaviour not only on the magnitude of the initial disturbance, but also on its spatial distribution. This result is consistent with that of Dauchot and Manneville (1997) obtained using a simplified nonlinear model which mimics the behaviour of the Navier-Stokes equations in a subcritical regime.

When $K_2^R < 0$ (near $\alpha = \alpha_B$ in Fig. 1(a)), for reasons which are discussed in Section 4 the physical relevance of the CGLE solution is limited to small times. Such solutions are typically discarded completely and are not discussed in the fluid dynamics literature. Nevertheless we believe they provide valuable qualitative insight into the initial development of disturbances. The formal solution dynamics is much more complicated when $K_2^R < 0$ as seen from Fig. 3. In this case the initially localised distribution leads to the appearance of two fronts. When $d > 0$ and $v_1 v_2 < 0$ (Fig. 3 (a)) the two fronts propagate in opposite directions and thus the solution decays asymptotically in the region between them. When $v_1 v_2 > 0$, the fronts move in the same direction (from left to right in Fig. 3 (b)), and asymptotically the solution will become finite at any point. However since the right front moves faster, an expanding region

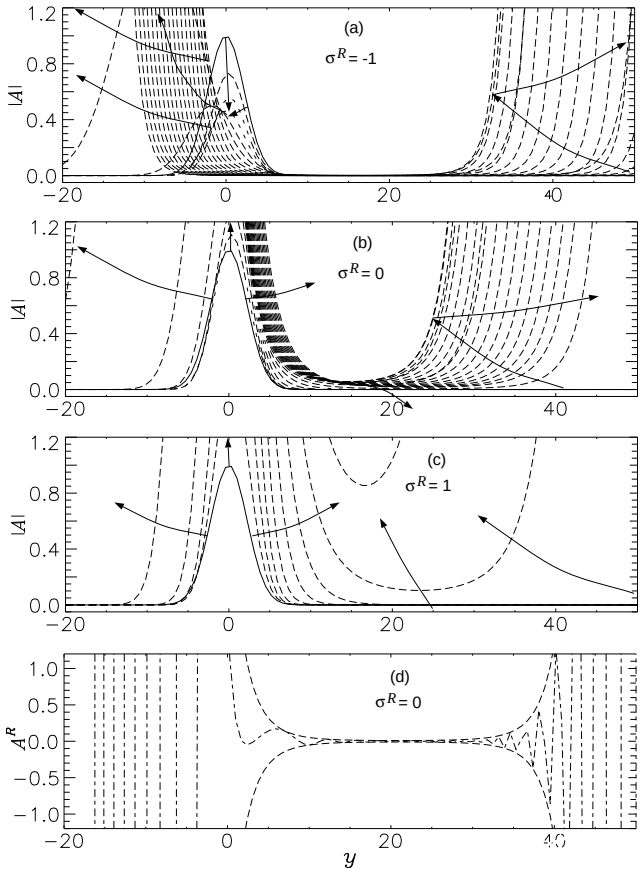


Fig. 3. Various solutions of the linear CGLE with negative $K_2^R$ with Gaussian initial condition for $c_g^I = K_2^R = -1$, $c_g^R = K_2^I = 1$, $v = 0$ and $a = 0.1$: $t = 0$ (solid lines) to $t = 10$ (dashed lines) with $\Delta t = 0.4$. Arrows show the directions of front propagations. Plot (d) illustrates the spatial variation of the real part of the amplitude in (b) corresponding to $t = 3$.

with nearly zero amplitude will exist between the fronts. Finally, if $d < 0$, the two fronts generated by the initially localised distribution move towards each other, collide and the solution amplitude increases everywhere with time (see Fig. 3 (c)).

The major conclusion which follows from the above illustrations is that when the coefficient $K_2^R$ is negative the solution of CGLE can grow rapidly even if its linear amplification rate $\sigma^R < 0$. At first sight this seems non-physical. The deeper analysis presented next clarifies this apparent contradiction.

### *3.2 Wavenumber cascading*

All disturbance development scenarios discussed so far are based on the analysis of a spatially modulated disturbance envelope centred at wavenumber $\alpha$ which in general is not equal to $\alpha_A$ corresponding to the maximum linear

amplification rate.

Consider Fig. 1 (b) where the leading eigenvalues are given as functions of wavenumber for the non-Boussinesq convection problem. Clearly, $K_2^R(\alpha)$ is negative in the vicinity of $\alpha_B$, the local minimum of the $\sigma^R(\alpha)$ curve. The value of $\sigma^R(\alpha_B)$ is negative and according to standard linear stability theory the monochromatic disturbance wave with this wavenumber must decay. At the same time Fig. 3 shows a rapidly growing solution of the CGLE with coefficients evaluated in the vicinity of $\alpha_B$. Typically this paradox is used to advocate the irrelevance of the Ginzburg-Landau model away from the maximum of the marginal stability curve. However it is trivial to show that if initially the disturbance amplitude is uniform in space then one would observe a rapidly decaying solution of the CGLE equivalent to that of a plane wave decay predicted by linear theory of monochromatic waves. Only initial spatial modulation can lead to the somewhat counter-intuitive results obtained above. Consequently, the influence of modulation has to be understood first. Closer inspection of the solution of the CGLE in the case of $K_2^R < 0$ shows that it is characterised by rapid spatial oscillations with the wavelength quickly decreasing in the direction of amplitude growth (away from the centre of the picture in Fig. 3(d)). Therefore the CGLE predicts strong spatial modulation of the original $\alpha$-harmonic within the wave envelope modelled by this CGLE when $\alpha \neq \alpha_A$. As a result the effective wavenumber of such solution changes with time so that a disturbance with a slower decay rate appears, see the arrow in Fig. 1 (b). This new harmonic, with an effective wavenumber located closer to $\alpha_A$, eventually dominates the original one and in turn, after being modulated itself, generates another harmonic with wavenumber closer to $\alpha_A$ (with even slower decay rate) and gets enslaved by it. This process continues until the disturbance with wavenumber $\alpha_A$ is obtained (lines $A$ in Fig. 1 a). In other words, spatial modulation of the initial disturbance wave gives rise to a slower overall decay rate than that expected for a monochromatic wave with the chosen wavenumber $\alpha \neq \alpha_A$ while the effective wavenumber cascades towards $\alpha_A$. Any initial modulation triggers such wavenumber change which is manifested through the positive combined temporal amplification rate (14) even when $\sigma^R(\alpha) < 0$. The detailed discussion of the Benjamin-Feir instability of noncritical waves performed in Suslov (1997) leads to the same conclusion: the side-band instability necessarily shifts the effective wavenumber to $\alpha_A$ regardless of the initial wavenumber. This puts the concept of wavenumber cascading introduced above on a firm ground but the extent of algebraic detail involved in such an analysis prohibits us from presenting it here. This shows that even though the coefficients of the CGLE are evaluated at a specific wavenumber $\alpha$, it contains information about a wider spectrum of disturbances. It will be shown in the Section 4 that it is the accuracy of this information what determines the relevance of the model for specific applications.

## 4 Relevance of the CGLE and its particular solutions to physical problems

The discussion in the previous sections shows how disturbances of arbitrary wavenumbers develop to those near $\alpha_A$ as a result of wavenumber cascading at the earlier stages of their evolution. In this section an important consequence of the above analysis will be introduced: we will develop a straightforward test which allows one to assess the range of applicability of the CGLE model without comprehensive comparisons with numerical solutions of a full problem. It will be shown to work well in the differentially heated cavity problem in Section 5.1.

In contrast to the cubic Landau amplitude equation, whose range of validity is discussed in detail in Suslov and Paolucci (1997b), the CGLE attempts to account for the disturbance wave envelope dynamics in a dispersive medium. The dispersion relation corresponding to the linearised version of the CGLE derived for a particular set of physical parameters and $v = 0$ is

$$\sigma_{\rm GL}(\beta;\alpha_0) = \sigma(\alpha_0) - {\rm i}c_g(\alpha_0)\beta - K_2(\alpha_0)\beta^2\,, \tag{21}$$

where $\alpha_0$ is the wavenumber at which the coefficients of the formally derived CGLE are evaluated ($\alpha_0 \neq \alpha_{A,B}$ in general) and $\beta$ is the modulation wavenumber for the fundamental wave with wavenumber $\alpha_0$. The relation (21) is quadratic in $\beta$ and thus is expected to be a good approximation to the physical dispersion relation only for small values of $\beta$ so that terms proportional to higher powers of $\beta$ are negligible (Suslov, 1997; Büchel and Lücke, 2000). On the other hand, if the physical dispersion relation itself is quadratic, for example,

$$\begin{aligned}\sigma(\alpha) =& C_1(\alpha_{A(B)} - \alpha)^2 + \sigma^R_{A(B)} \\ &+ {\rm i}\left[C_2(\alpha_{A(B)} - \alpha)^2 + c^R_{gA(B)}(\alpha_{A(B)} - \alpha) + \sigma^I_{A(B)}\right]\,,\end{aligned} \tag{22}$$

where all coefficients are real and subscript $A(B)$ corresponds to $C_1 < 0$ ($C_1 > 0$). Using (22) in (B.8) and (D.9) we obtain

$$\begin{aligned}c_g(\alpha) &= c^R_{gA(B)} + 2C_2(\alpha_{A(B)} - \alpha) + 2{\rm i}C_1(\alpha - \alpha_{A(B)})\,, \\ K_2(\alpha) &= -C_1 - {\rm i}C_2\,,\end{aligned} \tag{23}$$

so that subsequently we have

$$\begin{aligned}\sigma_{\rm GL}(\beta;\alpha_0) =& C_1(\alpha_{A(B)} - \alpha_0 - \beta)^2 + \sigma^R_A \\ &+ {\rm i}\left[C_2(\alpha_{A(B)} - \alpha_0 - \beta)^2 + c^R_{gA(B)}(\alpha_{A(B)} - \alpha_0 - \beta) + \sigma^I_{A(B)}\right].\end{aligned}$$

This dispersion relation is identical to the dispersion relation (22) for the full problem with $\alpha = \alpha_0 + \beta$. In other words, the modulated solution of

the linearised Ginzburg-Landau model fully recovers the linearised evolution of the solution amplitude of the complete problem no matter what value of wavenumber the model coefficients are evaluated at and/or whether $C_1$ (or, equivalently, $K_2^R$) is negative or positive as long as the physical dispersion relation is given by (22). Note though that $C_1 > 0$ in (22) obviously assumes the existence of arbitrarily fast growing disturbances with wavenumbers sufficiently far away from $\alpha_B$. This is unrealistic. Thus there can exist no physical problem whose full dispersion relation is given by (22) with $C_1 > 0$. In other words, even if the physical dispersion relation is locally such that $C_1 > 0$, there must exist an inflection point of the $\sigma^R(\alpha)$-curve where the sign of $C_1$ changes. At that point the physical dispersion relation necessarily deviates from quadratic (22) and the CGLE becomes irrelevant. We emphasise that the irrelevance of the CGLE in this case has nothing to do with the choice of $\alpha_0$ and how far it is from $\alpha_A$, but rather it is associated with the inadequacy of expression (22) to represent the physical dispersion relation. This means that the Ginzburg-Landau model with coefficients evaluated at $\alpha_0$ near $\alpha_B$ can only be accurate for relatively short time. Indeed, because of the cascading of the disturbance wavenumber towards faster growing waves discussed in Section 3.2, the effective wavenumber $\alpha_0 + \beta$ reaches eventually the inflection point of the $\sigma^R(\alpha)$-curve and invalidates the CGLE with negative $K_2^R(\alpha)$ for large time. On the other hand, if the physical dispersion relation is locally such that $C_1 < 0$ then the $\sigma^R(\alpha)$-curve has a finite maximum towards which the disturbance wavenumber approaches. The corresponding CGLE remains relevant as long as the wavenumber spectrum of the disturbances is limited to the interval between the inflection points of the $\sigma^R(\alpha)$-curve containing $\alpha_A$. Then, if the long time spatio-temporal dynamics of the physical flow is investigated, the CGLE predictions may only be valid if the contribution of the disturbance spectrum with wavenumbers near the inflection points of the $\sigma^R(\alpha)$-curve are asymptotically negligible. In other words the necessary condition for the accuracy of the long-term CGLE predictions is that $\sigma^R(\alpha) < 0$ at the inflection points (if they exist) of the physical dispersion relation. This is not a sufficient condition though. Indeed, if for example, the convective/absolute instability nature of the flow is studied, then all linearly amplifying disturbances contribute to the long-term evolution. Consequently, (21) has to be accurate for the complete range of $\alpha$ for which $\sigma^R > 0$. This is rarely the case for realistic flows and even if the inflection points are not present or correspond to negative linear amplification rates, the $\sigma^{R,I}(\alpha)$-curves frequently deviate from the parabolic shape. This is the reason why, for example, the convective/absolute instability boundary for mixed Boussinesq Rayleigh-Bénard-Poiseuille convection found in Müller et al. (1993) using the Ginzburg-Landau model disagrees with the one computed in Carrière and Monkewitz (1999) using the complete dispersion relation.

It is clear then that the CGLE can be used reliably in supercritical regimes, and in particular to predict accurate transition to absolute instability, only

when the full physical dispersion relation is very close to (22) with $C_1 < 0$ over the complete range of amplifying disturbances. If this is the case then substituting (23) into (16) and (17) we obtain that the coordinate system, with respect to which the maximum temporal amplification rate is observed always moves with speed $v_m(\alpha) = c_{gA}^R$, which is the group speed evaluated at $\alpha_A$. The effective amplification rate in this frame is $\gamma_m(\alpha) = \sigma_A^R$, the maximum amplification rate according to standard temporal linear stability theory. From (18) we then obtain that $d(\alpha) = -4C_1\sigma_A^R$, i.e. the flow is unstable whenever $\sigma_A^R > 0$. Since it follows from (15) that $\gamma_0(\alpha) = \sigma_A^R + C_1 c_{gA}^R / (C_1^2 + C_2^2)$, absolute instability can only occur in a medium with sufficiently small wave group speed. This is consistent, for example, with the results of Deissler (1987) who shows that instability in plane Poiseuille flow, for which the group speed is proportional to the Reynolds number and is relatively large, is always convective. Equation (20) provides an estimate of the disturbance spread rate $\tilde{v}(\alpha) = 4\sqrt{-\sigma_A^R (C_1^2 + C_2^2) / C_1}$ which grows with the temporal amplification rate. This shows once again why absolute instability generally occurs in more supercritical regimes: the disturbance extension rate has to become sufficiently large in order to overcome the wave envelope drift with the group speed. This can only occur if $\sigma_A^R$ is sufficiently large, i.e. further away from the marginal stability surface.

All results noted above are independent of the actual value of $\alpha_0$ at which the CGLE is derived. This leads to a straightforward conclusion: if the dispersion relation for the full physical problem is parabolic, then the long-term flow behaviour predicted by the CGLE does not depend on the actual wavenumber $\alpha_0$ for which its coefficients are evaluated: it will be identical to that of the model with coefficients evaluated at $\alpha_0 = \alpha_A$. For this reason it is convenient to evaluate all coefficients at this wavenumber from the start as the extent of algebraic detail in this case is the least. In Section 5 we also take advantage of this fact and conveniently compute all coefficients at $\alpha_A$ unless specified otherwise. Nevertheless, it would be unwise to discard completely the consideration of the CGLE with coefficients evaluated at $\alpha_0 \neq \alpha_A$ for two reasons. First, it sheds light on the non-trivial mechanism of wavenumber change at the earlier stages of disturbance development, especially when the spectrum of the initial disturbance envelope does not involve the $\alpha_A$-harmonic. Secondly, and most importantly, it provides a way of judging the accuracy of the CGLE predictions as discussed below.

The accuracy of the CGLE results is easily assessed by computing the $\sigma^{R,I}(\alpha)$ curves for a particular problem. If these curves are parabolic for the complete range of wavenumbers corresponding to positive linear amplification rates $\sigma^R(\alpha) > 0$ then the use of the CGLE produces reliable results, otherwise a different type of analysis must be invoked. Such a test is simple and inexpensive in comparison with commonly used direct numerical simulations of a full nonlinear problem or experimental investigation as done, for exam-

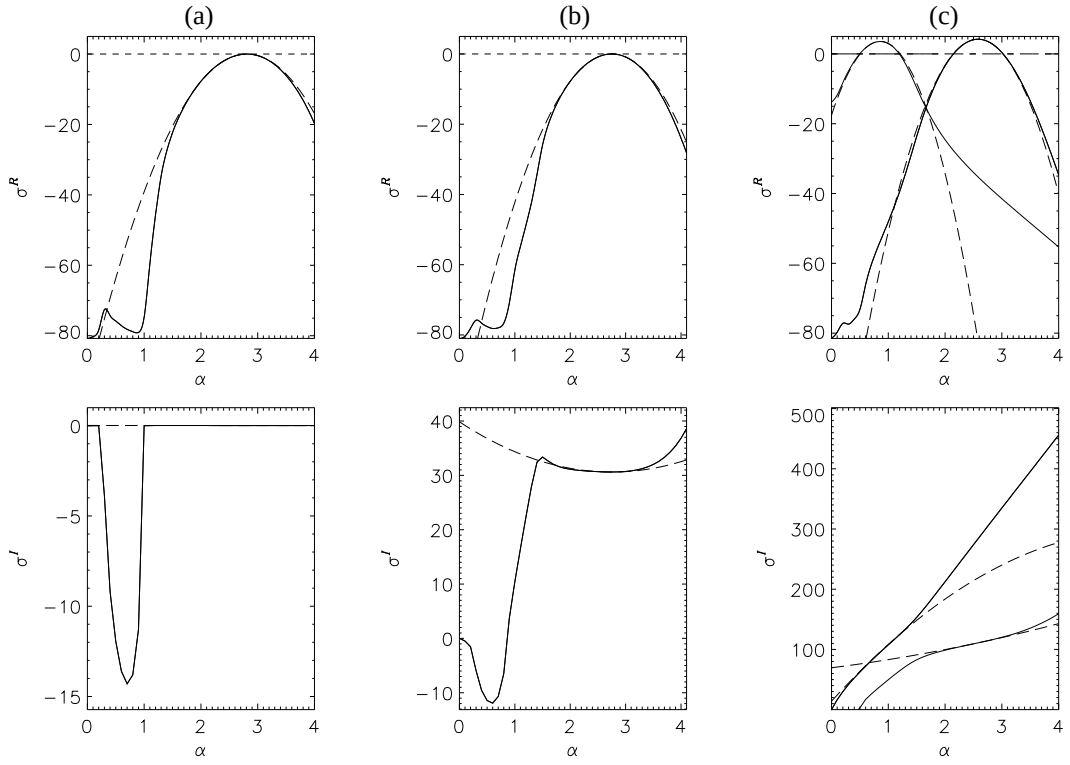


Fig. 4. Comparison of the full numerical (solid lines) and approximate quadratic (CGLE) (dashed lines) dispersion relations along the boundary separating the regions of convective and absolute instabilities in the natural convection problem in (a) the Boussinesq limit $\epsilon \to 0$, $Gr = 8037$, (b) $\epsilon = 0.3$, $Gr = 9273$ and (c) $\epsilon = 0.6$, $Gr = 16817$. The coefficients of the CGLE are evaluated at $\alpha_A$.

ple, in Büchel and Lücke (2000) and Büchel et al. (1996), respectively. The test involves solving only the linear algebraic eigenvalue problem (B.2) for a range of values of (real) wavenumber $\alpha$ and plotting the leading eigenvalue(s). In Fig. 4 we show the result of applying such a procedure to the problem of non-Boussinesq natural convection defined in Section 2. Since the parabolic approximation (dashed line) is virtually indistinguishable from the dispersion relation (B.5) of the full problem (solid line) for the complete range of wavenumbers with $\sigma^R(\alpha) > 0$, the application of the CGLE is well justified. In particular, the convective/absolute instability boundary is given very accurately by the CGLE analysis. Although not presented here, our computation of convective/absolute instability transition for natural convection at selected values of the temperature difference $\epsilon$ between the walls using the analysis of complex saddle points of the numerical dispersion relation (see Huerre and Monkewitz, 1990) shows agreement with the CGLE analysis to within 1.3%. On the other hand, tests for convection with through-flow show that the corresponding $\sigma(\alpha)$ curves are not parabolic. Consequently, the application of the CGLE is not justified for mixed or forced convection regimes as was also empirically noted in Carrière and Monkewitz (1999) and Büchel and Lücke (2000).

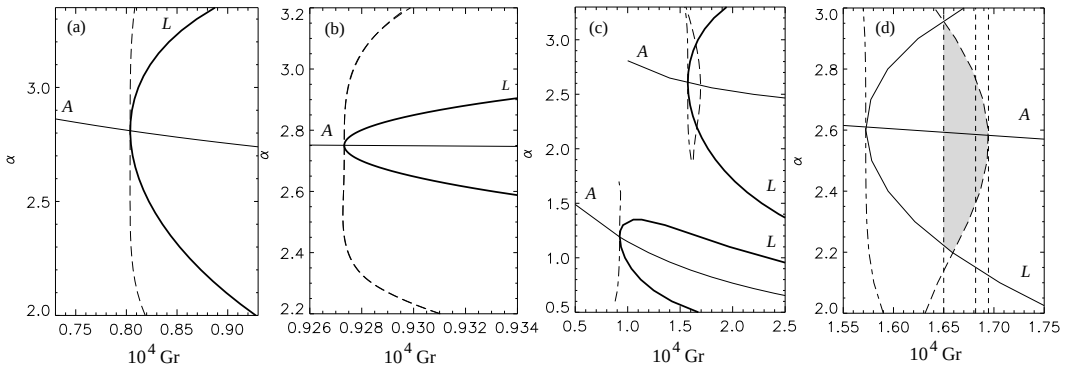


Fig. 5. Modified stability diagrams for (a) $\epsilon = 0.005$, (b) $\epsilon = 0.3$, (c) $\epsilon = 0.6$ and (d) close-up of (c). Long-short dash and dashed lines represent the boundaries of convective ($\gamma_m = 0$) and absolute ($\gamma_0 = 0$) instabilities, respectively. $L$: linear stability boundary ($\sigma^R = 0$); $A$: line of the maximum linear amplification rate $\sigma^R$.

## 5 Results

Encouraged by the accuracy test for the CGLE in Section 4, we now apply the general theoretical procedure to non-Boussinesq natural convection flow of air in a tall cavity. All numerical results were obtained using 52 Chebyshev spectral modes (see Suslov and Paolucci, 1995a, for the description of the numerical approximation) and double precision versions of appropriate IMSL Inc. (1989) routines: NEQNF to solve for the basic flow, GVCCG and GVLRG to solve the generalised eigenvalue problem for $\alpha > 0$ and $\alpha = 0$ respectively, LSBRR to solve the mean flow correction equations, LSACG to solve the equations for the second harmonic and for $\boldsymbol{\chi}$, and LSVCR to solve for the spatially modulated distribution $\boldsymbol{w}_{21}$ (see Appendices C and D).

### *5.1 Convective vs absolute instability in non-Boussinesq natural convection*

The coefficients entering the CGLE (12) depend not only on the physical parameters such as the Grashof number, the Prandtl number, and the temperature difference between the walls, but also on the chosen wavenumber $\alpha$. As discussed in Section 4, such dependence results in equivalent asymptotic behaviours regardless the wavenumber at which the model coefficients are evaluated, but only if the physical dispersion relation $\sigma(\alpha)$ is quadratic. This is a condition for the validity of the CGLE. Here we discuss this criterion from a slightly different angle. We look at the linear stability diagrams presented in Fig. 5 for different values of the temperature difference between the walls. The lines $L$ represent the standard linear stability boundary $\sigma^R(\alpha, \mathrm{Gr}) = 0$ for monochromatic waves. Spatial modulations modify it. The more realistic stability diagrams accounting for modulations are produced by analysing the equivalent CGLE model derived for arbitrary $\alpha$ and applying criteria

$\gamma_m(\alpha, \mathrm{Gr}) = 0$ for the convective instability boundary and $\gamma_0(\alpha, \mathrm{Gr}) = 0$ for the absolute one; see the long-short dash and dashed lines in Fig. 5. These modified diagrams take into account the wavenumber cascade discussed in Section 3.2. If the physical dispersion relation is quadratic then, as shown in Section 4, criteria (14) and (15) are $\alpha$-independent and both $\gamma_m = 0$ and $\gamma_0 = 0$ would be represented by vertical lines in Fig. 5. The extent of such straight-line instability boundaries shows the validity range of the Ginzburg-Landau approximation. Deviation of the instability boundaries from straight vertical lines in Fig. 5 corresponds to the ranges of wavenumbers in Fig. 4 where distinction between the physical (solid lines) and model (dashed lines) dispersion relations are clearly seen (for negative amplification rates). The CGLE model performance is expected to be satisfactory if lines $\gamma_m = 0$ and $\gamma_0 = 0$ have vertical linear segments across the complete range of wavenumbers with $\sigma^R(\alpha) > 0$, i.e. within the region bounded by the linear instability line $L$ in Fig. 5. This is surely the case for Boussinesq and weakly non-Boussinesq natural convection flows, see Fig. 5 (a) and (b), respectively. In these regimes the CGLE provides excellent results for transition to absolute instability. On the other hand, when the symmetry-breaking effects of fluid property variations with temperature become very strong the disturbance group speed increases. This in turn leads to transition at a larger value of Grashof number and deviation of the physical dispersion relation from quadratic: the dashed line within curve $L$ in Fig. 5 (c) is not straight anymore indicating that the accuracy of the CGLE results has deteriorated. In fact all one can say is that the transition to absolute instability occurs somewhere within the shaded region in Fig. 5 (d) between the vertical dotted line through the leftmost intersection of the dashed and solid ($L$) lines and the rightmost vertical dotted line tangent to the dashed line. In other words in this case the application of the Ginzburg-Landau theory only gives an estimate of the transitional Grashof number $\mathrm{Gr} = 16725 \pm 225$. Indeed the accurate value of the Grashof number corresponding to transition to absolute instability which we computed using the saddle point method (see Huerre and Monkewitz, 1990) for $\epsilon = 0.6$ is found to be 16817 (middle vertical dashed line in Fig. 5 (d)) is well within the range predicted by CGLE. The discrepancy between the accurate and estimated values is noticeable, but the relative error of the CGLE estimate does not exceed 1.3%. The model is still reasonably accurate, consistent with the conclusion made in Section 4 based on Fig. 4 (c). The above example shows how a reasonable estimate of the accuracy of the CGLE predictions can be obtained if its coefficients are computed for a range of the wavenumbers in the vicinity of that providing the maximum linear amplification rate. This accuracy estimate requires significantly less resources than comparison with experimental, DNS or complete saddle point analysis. Remarkably, a quantitative error bound estimate is not possible in principle if only the CGLE with coefficients evaluated at $\alpha_A$ is considered.

As follows from Fig. 4 (a), $\sigma^I = 0$ when $\sigma^R > 0$, i.e. the disturbances are

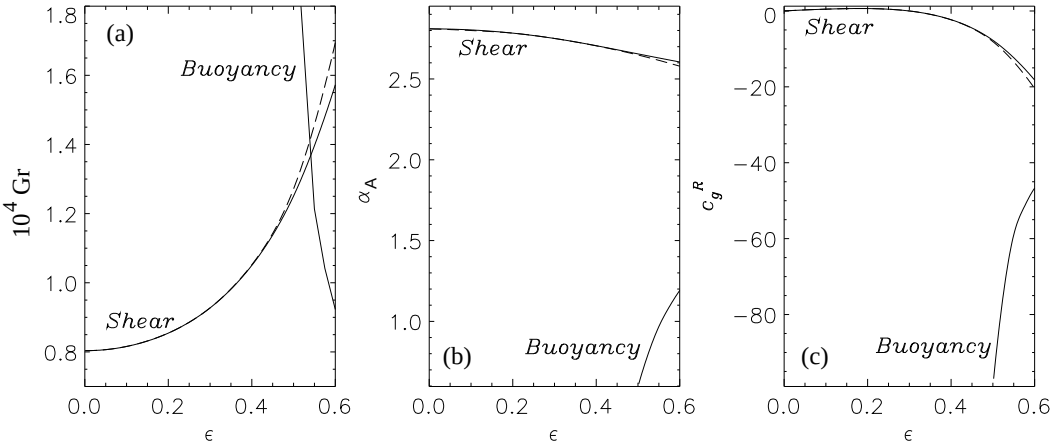


Fig. 6. (a) Convective/absolute instability transition diagram: the flow is linearly stable below the solid line, absolutely unstable above the dashed line and convectively unstable between them; (b) wavenumber $\alpha_A$ corresponding to the largest temporal amplification rate $\sigma^R$ and (c) disturbance group speed $c_g^R$ along the stability boundaries shown in (a).

stationary in Boussinesq natural convection. Then $c_g^R = K_2^I = 0$ and thus conditions $d = 0$ (see (18)) and $\gamma_0 = 0$ define the same curve. In other words, convective instability cannot be observed in a system where disturbances are of standing-wave type; there the linear instability is necessarily absolute. Similarly, as seen in Fig. 4 (b), $c_g^R \approx 0$ for weakly non-Boussinesq convection (the slope of the $\sigma^I(\alpha)$-curve is close to zero near the maximum of $\sigma^R(\alpha)$). Therefore transition to absolute instability occurs at a value of the Grashof number which is very close to that of linear instability (the dashed and long-short dash lines cannot be distinguished in Fig. 5 (b)). In contrast, in strongly non-Boussinesq regimes the slope of the $\sigma^I(\alpha)$-curve is finite (see Fig. 4 (c)), $c_g^R \neq 0$ and the distinction between the linear and absolute instability boundaries for the shear mode (the upper branch in Fig. 5 (c), see Suslov and Paolucci (1995b)) is clearly seen. The buoyancy driven instability occurring in strongly non-Boussinesq flows (lower branch in Fig. 5 (c)) remains of convective type for values of Grashof number at least up to $3 \times 10^4$. This is consistent with the results of Suslov and Paolucci (1995b) who found that this type of instability occurs in the region of downward flow near the cold wall: plumes of overcooled fluid with larger density drop in the direction of gravity. Hence, buoyant disturbances generated near the top end of the cavity can only propagate downwards, and this determines the convective character of instability.

A complete convective/absolute instability transition diagram for various values of temperature differences between the walls is shown in Fig. 6 (a). Fig. 6 (c) shows the disturbance group speed $c_g^R$. It is zero in the Boussinesq limit $\epsilon \to 0$ and this explains why in this case the instability is absolute: disturbances are not carried away by the primary flow and are observed in a stationary frame.

The specific non-Boussinesq fluid property variations (6)–(8) break the symmetry of the primary flow so that the disturbance group speed first becomes slightly positive reaching its maximum of about 0.64 at $\epsilon \approx 0.2$ and then decreases rapidly crossing zero at $\epsilon \approx 0.3$ and becomes negative for larger values of the temperature difference between the walls. This is because the shear disturbances begin to develop closer to the cold wall where the flow is downward. This explains why the region of convective instability exists for larger temperature differences between the walls. The buoyancy disturbances existing in strongly non-Boussinesq flows are characterised by much smaller wavenumbers (see Fig. 6 (b)), faster group speeds and relatively small temporal amplification rates and for this reason the buoyancy driven instability remains of convective type.

### *5.2 Comparison of numerical results of the CGLE with DNS*

All analysis and results presented thus far have been obtained for an essentially infinitely tall enclosure so that the influence of the top and bottom walls only enter through the enforcement of global mass conservation (9). Obviously such a configuration is a mathematical abstraction. Nevertheless in this section we show the analytical results for the simplified infinite geometry are in full qualitative and quantitative agreement with the realistic flow existing in a tall but finite enclosure sufficiently far from the ends, thus justifying the weak influence of the distant boundary conditions in the CGLE model.

In all regimes investigated, results of comprehensive linear stability analysis (Suslov and Paolucci, 1995b) show that the instability remains two-dimensional with convection roll axes along the span-wise direction. Therefore, as a final step in justifying the accuracy of the results presented in the previous section, we obtain DNS results of the two-dimensional flow in a closed cavity of aspect ratio $A_H = 40$ using the finite volume code described in Chenoweth and Paolucci (1986) with spatial discretisation of $51 \times 301$ points. Selected DNS simulations were also performed for cavity of aspect ratio $A_H = 50$ to demonstrate that the patterns arising in the middle part of the cavity are fully consistent with those obtained for $A_H = 40$ and therefore to conclude that the influence of the finite enclosure size is negligible in the context of the present investigation. The CGLE was solved numerically with linear terms discretised using the Crank-Nicolson scheme while the nonlinear term was treated explicitly using the second order Adams-Bashforth scheme. The CGLE time integration step was $\Delta t = 5 \times 10^{-4}$ and the spatial discretisation step was $\Delta y = 4 \times 10^{-2}$.

The DNS was started with a motionless isothermal state at $T = 1$. The fluid accelerates quickly along the differentially heated walls by buoyancy

forces, then it hits the horizontal top and bottom walls which force it to turn. Thus, the distant top and bottom ends act as natural sources of (finite amplitude) disturbances to the parallel basic flow existing in the middle part of the cavity (Chenoweth and Paolucci, 1985). Consequently, in order to mimic this scenario, when solving the equivalent CGLE we take $A(y,0) = a_0 \int_0^{A_H} [\delta(y-A_H+\tilde{y})-\delta(y-\tilde{y})]\,\mathrm{d}y$, where $A_H$ is the dimensionless cavity height, $a_0$ is the amplitude of the initial pulse, $\tilde{y}$ is its initial location (all numerical results are obtained for $\tilde{y} = 0.03A_H$), $\delta(y)$ is the Dirac delta function, and we enforce the boundary conditions $A(0,t) = A(A_H,t) = 0$. These conditions are chosen to mimic the physical no-slip/no-penetration conditions for velocities. Of course, these conditions are not rigorous since they are imposed in regions where the amplitude equation itself is not appropriate as it is based on the parallel basic flow assumption which does not exist near the ends. Although we have argued in the Introduction that disturbance reflections from the walls can be neglected in this problem the global effect of the above zero boundary conditions cannot. The disturbance mechanical energy loss at the boundaries delays the transition to absolute instability associated with the appearance of an unstable global mode (Huerre and Monkewitz, 1990) in this case. It occurs at a larger value of the governing parameter (the Grashof number in this case) to compensate for this energy loss (Cross and Kuo, 1992, see the qualitative discussion therein). Indeed, as shown by Tobias et al. (1998), the first global mode obtained by solving the linearised CGLE (1) with the above boundary conditions is

$$A(y,t) = \sin\left(\frac{\pi y}{A_H}\right) \mathrm{e}^{\tilde{\sigma}t + \frac{c_g^2}{2K_2}y}\,,\ \tilde{\sigma} = \sigma - \frac{c_g^2}{4K_2} - K_2\frac{\pi^2}{A_H^2}\,.$$

The condition $\gamma_0 = 0$ for the absolute instability boundary in the infinitely tall cavity results in $\tilde{\sigma}^R = -K_2^R\pi^2/A_H^2 < 0$ as $K_2^R > 0$ for $\alpha = \alpha_A$, i.e. the zero boundary conditions stabilise the flow. Thus the transition to absolute instability in a cavity of finite aspect ratio occurs at a larger Grashof number. This difference was found to be largest at $\epsilon = 0.6$. In this case the linear global mode amplification rate $\tilde{\sigma}^R$ is zero for $A_H = 40$ at $\mathrm{Gr} = 16989$ which is only 0.3% larger than the value of $\mathrm{Gr}_{\mathrm{abs}}$ reported in the previous section. Hence in the following discussion we do not distinguish between the global modes in the finite aspect ratio cavity from absolute instability in the infinitely tall closed cavity focusing on the regions away from the top and bottom ends. Tests for a cavity of aspect ratio $A_H = 50$ show that the predicted instability patterns observed near the cavity centre do not differ from those presented here for $A_H = 40$ confirming that the detailed influence of the remote top and bottom walls is insignificant in the context of the present study.

First, we justify the comparison between stability results for a parallel basic flow in the infinitely tall cavity with the DNS results for the cavity of aspect ratio 40. As seen from Fig. 7, the flow profiles which are quickly established in the middle part of a finite enclosure can hardly be distinguished from the

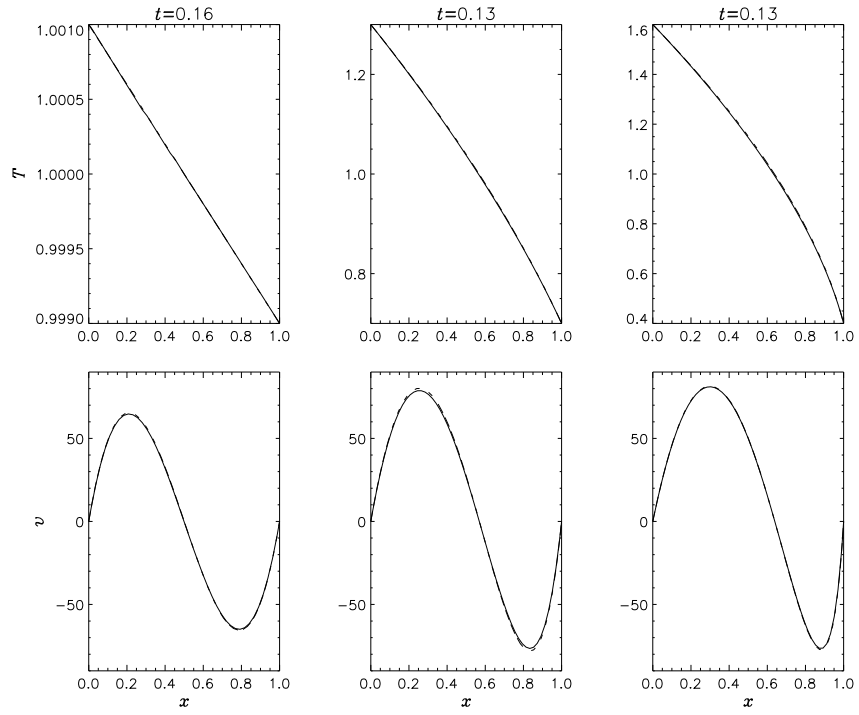


Fig. 7. Temperature (top) and vertical velocity component (bottom) profiles at $y = 20$ in a vertical cavity of aspect ratio 40 for $(\epsilon, \mathrm{Gr}) = (0.001, 8170)$ (left), $(\epsilon, \mathrm{Gr}) = (0.3, 9860)$ (middle), and $(\epsilon, \mathrm{Gr}) = (0.6, 9860)$. Solid lines represent DNS results, dashed lines correspond to spectral results for an infinitely tall cavity, at the times indicated.

spectral approximation in Suslov and Paolucci (1995b) for an infinitely tall cavity for all values of $\epsilon$. They remain unchanged until they become affected by the natural travelling disturbance waves arising from the flow turning at the top and bottom ends of the cavity. Therefore, the stability theory developed here for an infinitely tall enclosure is expected to be in reasonable agreement with the DNS results for a sufficiently tall cavity.

The major numerical results are summarised in three groups of figures below. Figs. 8–10 show the solutions of the CGLE which correspond to DNS results presented in Figs. 11–14. Details of the DNS results along the vertical mid-plane are given in Figs. 15–19.

For the slightly supercritical Boussinesq regime of $(\epsilon, \mathrm{Gr}) = (0.001, 8170)$ (the critical value of the Grashof number in this case is 8037) the constants entering the Ginzburg-Landau model are $\sigma \approx (0.765, 0.090)$, $c_g \approx 0.005$, $K_1 \approx (-1.22 \times 10^3, -3)$, and $K_2 \approx (12.1, -0.004)$, all evaluated at $\alpha_A \approx 2.802$. Fig. 8 shows that two disturbance wave envelopes, initially mimicking the flow-turning influence of the top and bottom cavity walls, move towards each other, eventually resulting in a nonzero solution in the complete domain. This situation corresponds to absolute instability as predicted by Fig. 6 (a).

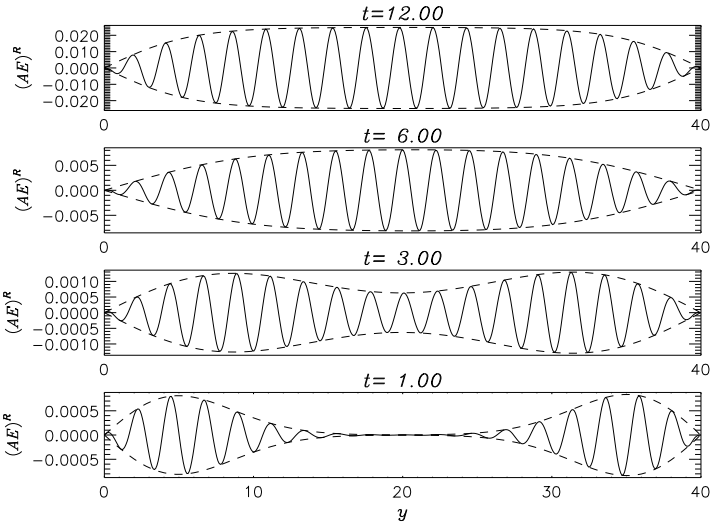


Fig. 8. Solutions of the CGLE for $(\epsilon, \mathrm{Gr}) = (0.001, 8170)$. The instability is absolute.

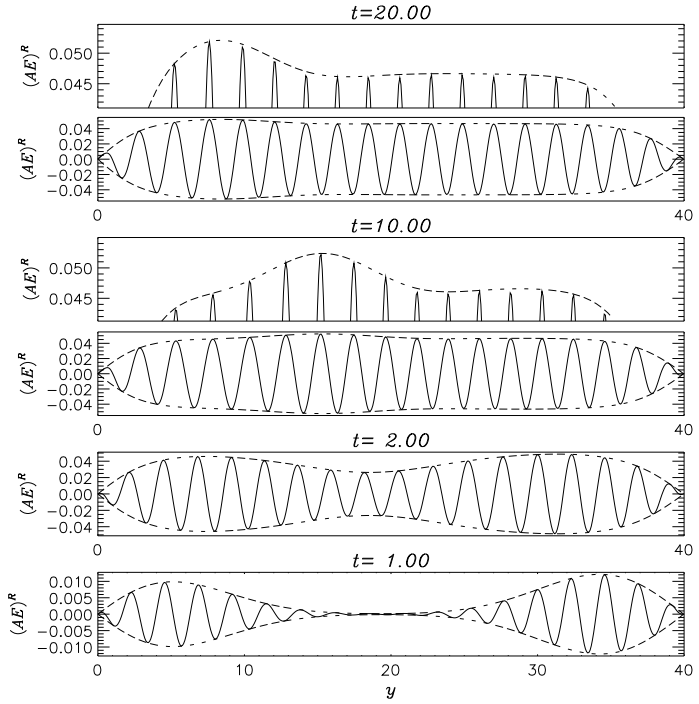


Fig. 9. Solutions of the CGLE for $(\epsilon, \mathrm{Gr}) = (0.3, 9860)$ with close-up views (the first and third plots from the top) of a solitary structure. The instability is absolute.

Snapshots of the DNS results presented in Fig. 11 and plots of the horizontal velocity component $u$ (which is zero for undisturbed parallel flow) in Fig. 15 confirm the above conclusions: the fully developed parallel basic flow is established in the middle part of the cavity and its instability starts developing by $t \approx 0.16$. The end regions, where the fluid flow turns, act as sources of disturbances to the parallel flow. These disturbances propagate towards the centre of the cavity (snapshots at $t = 0.33$ and $t = 0.82$), collide and form an essen-

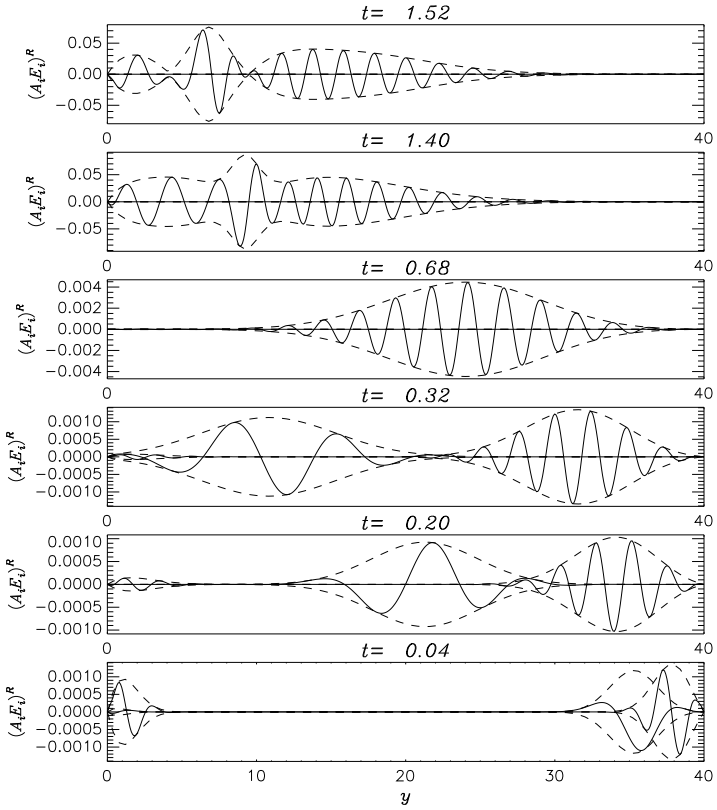


Fig. 10. Solutions of the coupled equations (26)–(27) for $(\epsilon, \mathrm{Gr}) = (0.6, 16900)$. The instability is linearly convective.

tially steady wavy flow with wavenumber $\alpha \approx 2.80$ which is estimated based on the average distance between the velocity peaks in Fig. 15. This value is in excellent agreement with the wavenumber of the maximum amplification rate predicted by linear stability analysis (see Fig. 6 (b)). The wavy flow occupies most of the cavity at $t = 5.68$ emphasising the absolute nature of instability.

In the supercritical weakly non-Boussinesq regime $(\epsilon, \mathrm{Gr}) = (0.3, 9860)$ (the critical Grashof number is 9273, see Fig. 5 (b)) the constants entering the CGLE are $\sigma \approx (3.03, 32.5)$, $c_g \approx -0.632$, $K_1 \approx (-1.08 \times 10^3, -1.29 \times 10^3)$, and $K_2 \approx (14.3, -1.12)$, all evaluated at $\alpha_A \approx 2.721$. The corresponding solution of the CGLE is presented in Fig. 9. As in the Boussinesq limit the two wave envelopes extend towards each other and eventually occupy the complete computational domain. Thus, as predicted by the analysis in Sections 3.1 and 5.1, the instability is absolute, but in this case there exists a direction of preferred propagation (the group speed $c_g$ is negative) which breaks the symmetry of the solution: the soliton-like structure propagates towards $y = 0$ as seen from the enlarged snapshots at $t = 10$ and $t = 20$ in Fig. 9. The

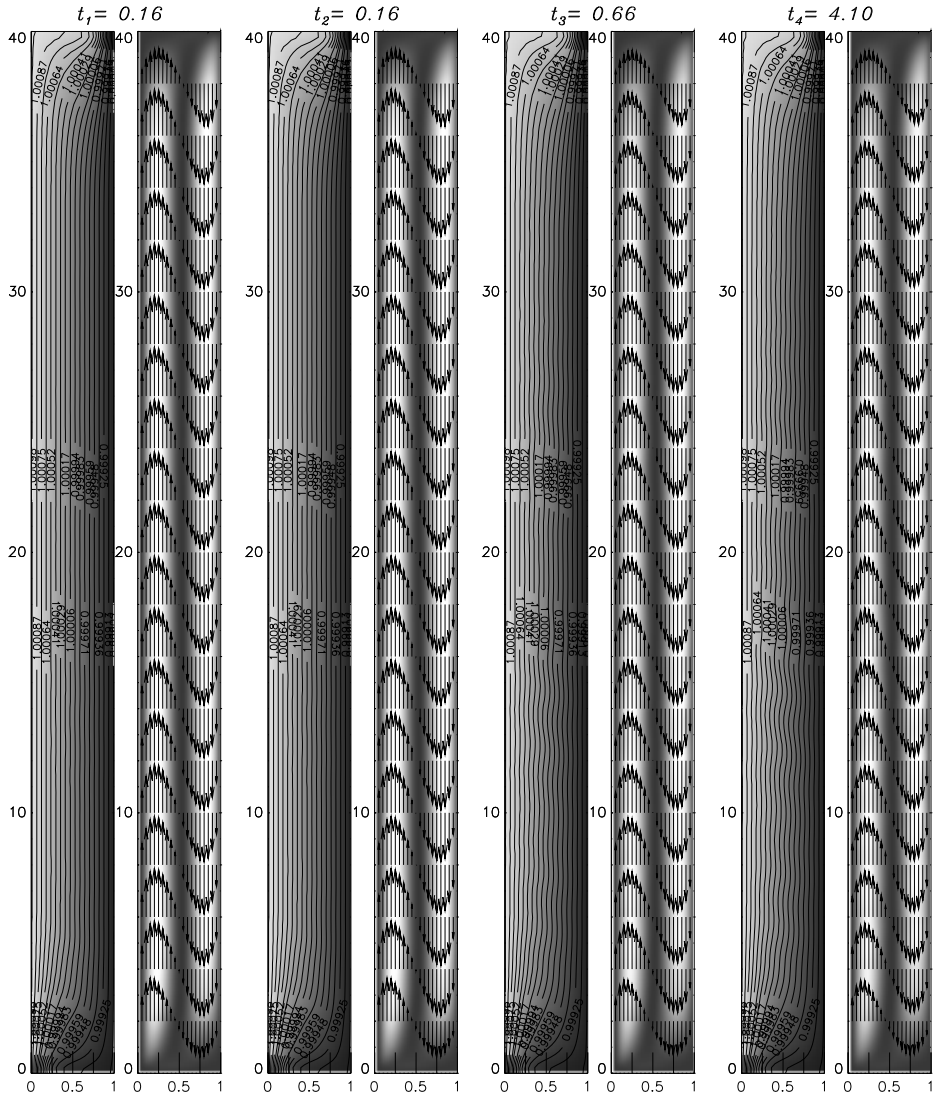


Fig. 11. Flow fields for $\epsilon = 0.001$ and Gr $= 8170$. Lighter regions in the thermal (left) and velocity (right) fields correspond to higher temperature and larger kinetic energy, respectively.

solitary solution of the cubic Ginzburg-Landau equation can be found in the polar form $A(t,y) = a(t,y)\mathrm{e}^{\mathrm{i}\theta(y,t)}$ with

$$a(t,y) = r\,\mathrm{sech}(b\eta), \quad r > 0\,,\ \eta = y - Vt\,, \tag{24}$$

$$\theta(t,y) = p\ln[\cosh(b\eta)] + ky + lt + \theta_0\,, \tag{25}$$

where

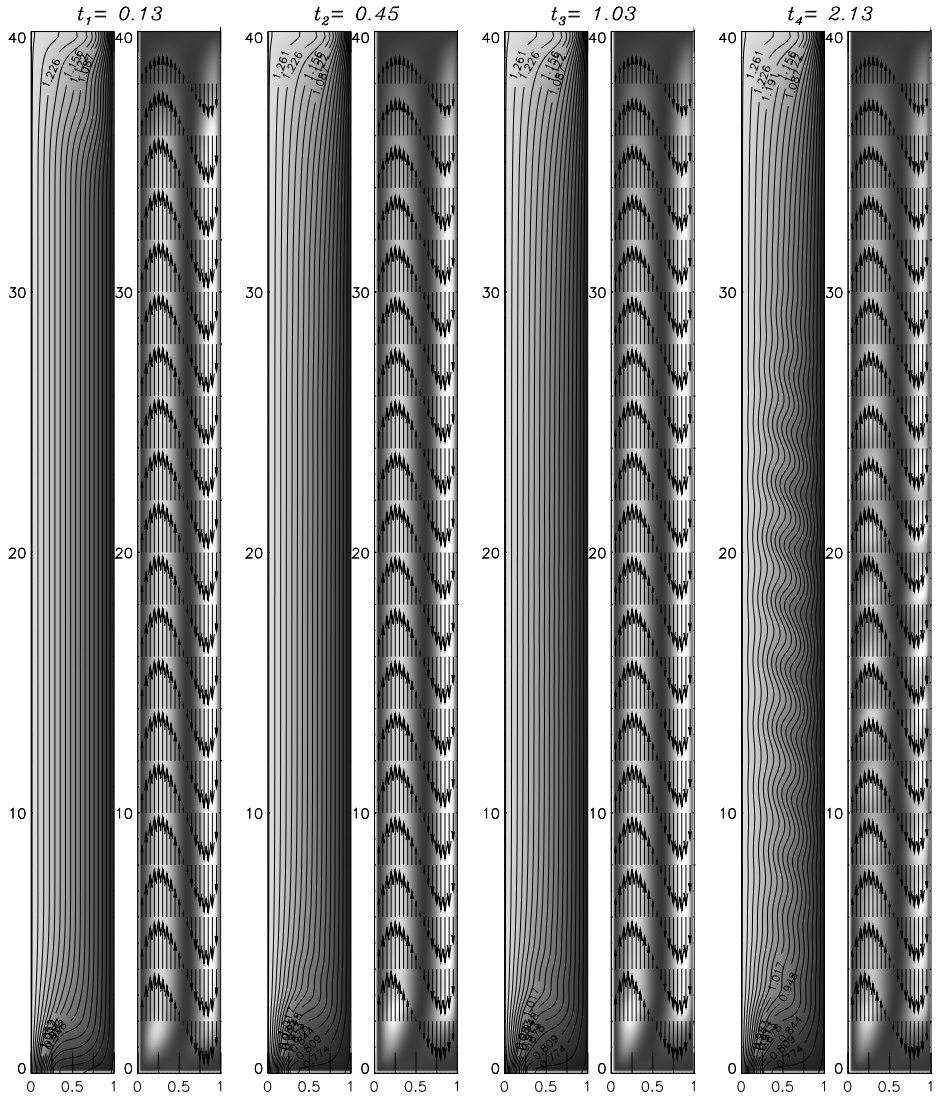


Fig. 12. Flow fields for $\epsilon = 0.3$ and $\mathrm{Gr} = 9860$. Lighter regions in thermal (left) and velocity (right) fields correspond to higher temperature and larger kinetic energy, respectively.

$$r^2 = 3\frac{pb^2|K_2|^2}{\lambda_2}\,, \quad b^2 = \frac{d}{4K_2^R\left[K_2^R\left(p^2-1\right)-2K_2^I p\right]}\,, \quad V = c_g^R + c_g^I\frac{K_2^I}{K_2^R}\,,$$

$$p = -\frac{3\lambda_1}{2\lambda_2}\left[1-\mathrm{sign}(\lambda_1)\left(1+\frac{8\lambda_2^2}{\lambda_1^2}\right)^{1/2}\right]\,,$$

$$\lambda_1 = K_1^R K_2^R + K_1^I K_2^I\,, \quad \lambda_2 = K_1^R K_2^I - K_1^I K_2^R\,.$$

$$k = \frac{c_g^I}{2K_2^R}\,, \quad l = b^2\left[K_2^I\left(1-p^2\right)-2K_2^R p\right] - K_2^I k^2\,.$$

This is a generalisation of the solitary wave solution given, for example, by

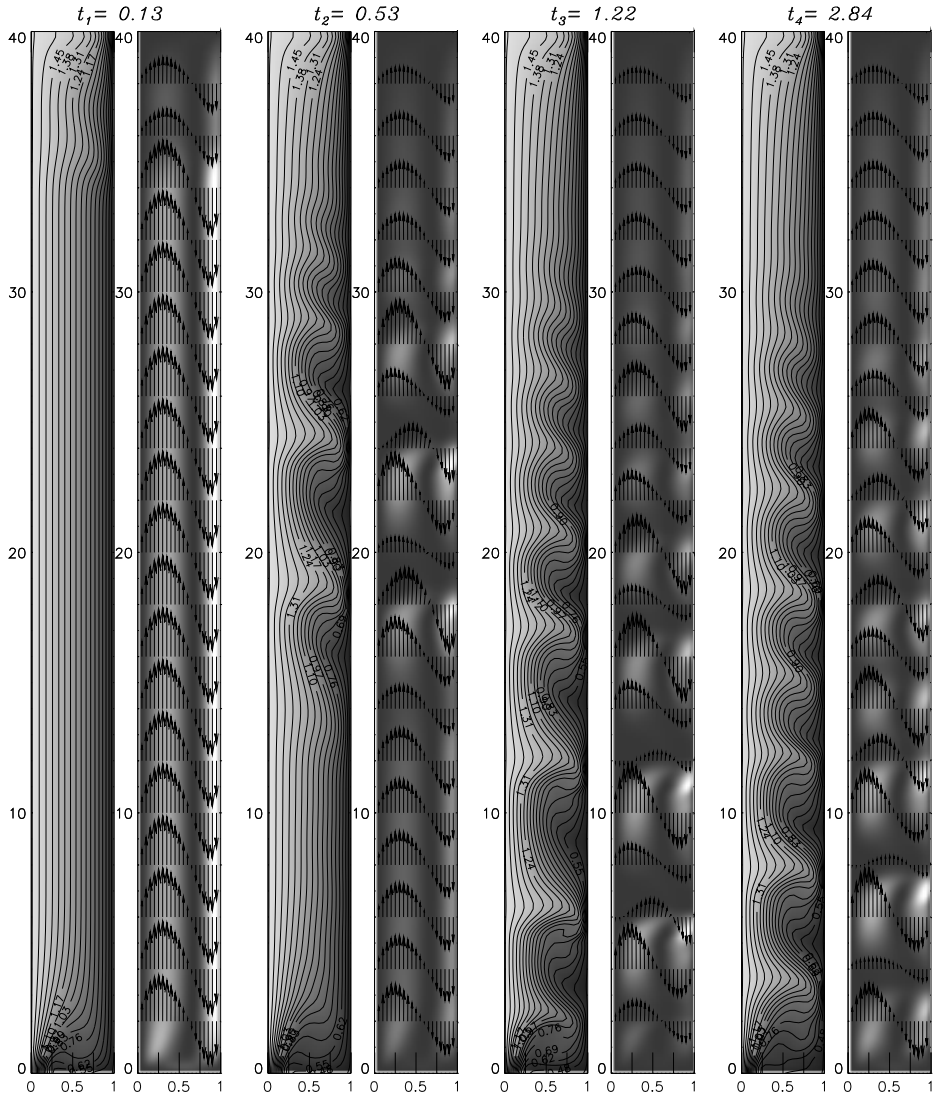


Fig. 13. Flow fields for $\epsilon = 0.6$ and $\mathrm{Gr} = 9860$. Lighter regions in thermal (left) and velocity (right) fields correspond to higher temperature and larger kinetic energy, respectively.

Newell (1974). For the above constants, (24) has amplitude $r \approx 0.052$ which is very close to the maximum amplitude of the solution shown in Fig. 9.

The DNS results presented in Fig. 16 also indicate the existence of the preferred downward direction of disturbance propagation (see sequence of snapshots $t = 0.13$, $t = 0.45$, and $t = 1.03$) and the absolute instability of the parallel basic flow ($t = 2.13$, see also Fig. 12). The initial overshoot of the horizontal velocity near the upper wall (seen at $t = 0.13$) creates a large amplitude disturbance which propagates downwards (see snapshot at $t = 0.45$). Its large wavelength seen in the region $25 < y < 35$ for $t = 0.45$ suggests that this disturbance is of buoyancy type. This is consistent with the linear

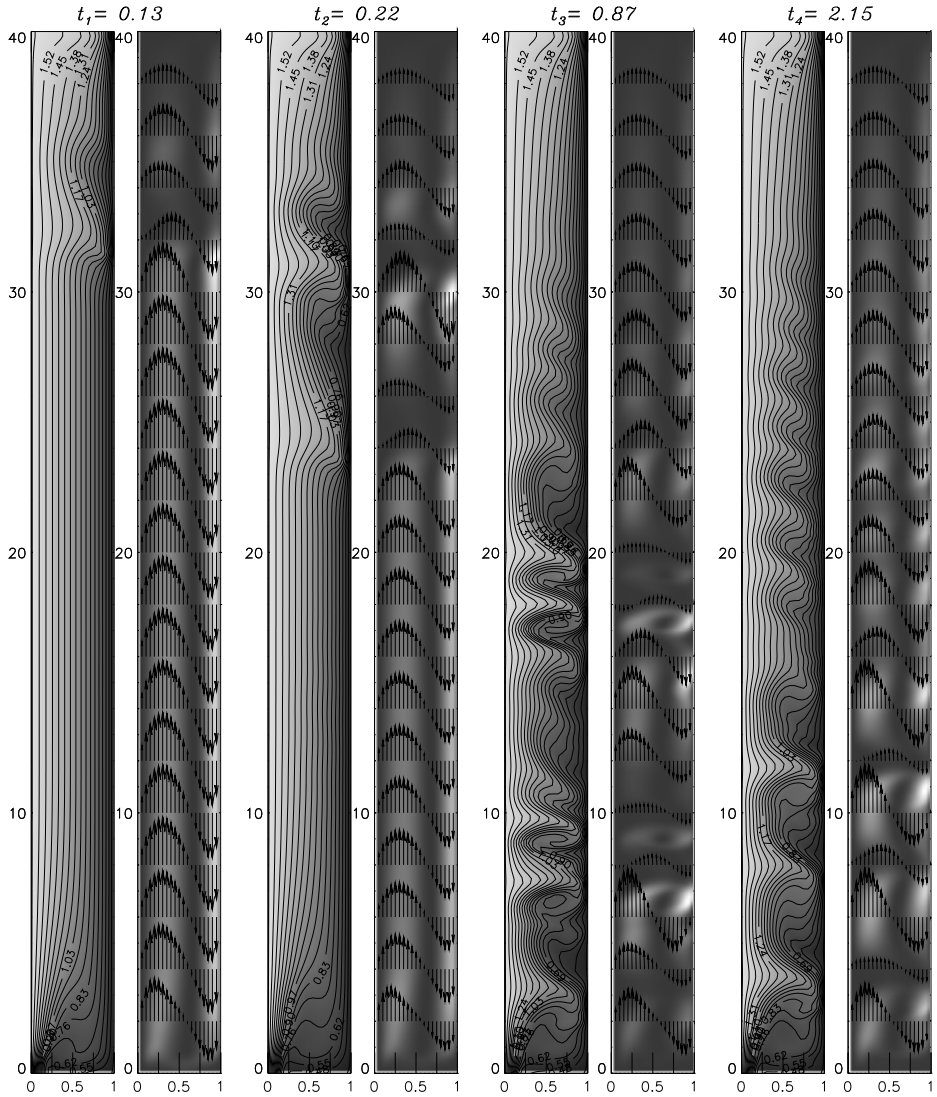


Fig. 14. Flow fields for $\epsilon = 0.6$ and $\mathrm{Gr} = 16900$. Lighter regions in thermal (left) and velocity (right) fields correspond to higher temperature and larger kinetic energy, respectively.

stability analysis which predicts negative amplification rate for the buoyancy mode in weakly non-Boussinesq regimes (see dashed line in Fig. 1 (b)) and its rapid decay. The initial velocity overshoot near the bottom of the cavity also creates a large amplitude disturbance, but because buoyancy disturbances are characterised by relatively large negative group speeds these disturbances do not propagate upwards. The two middle snapshots in Fig. 16 also illustrate the wavenumber cascading towards the most unstable one: according to linear analysis the initial long wave disturbance seen at $t = 0.45$ is replaced with a shorter linearly unstable shear one by $t = 1.03$. The development of the absolutely unstable shear instability is clearly seen in snapshots at $t = 1.03$

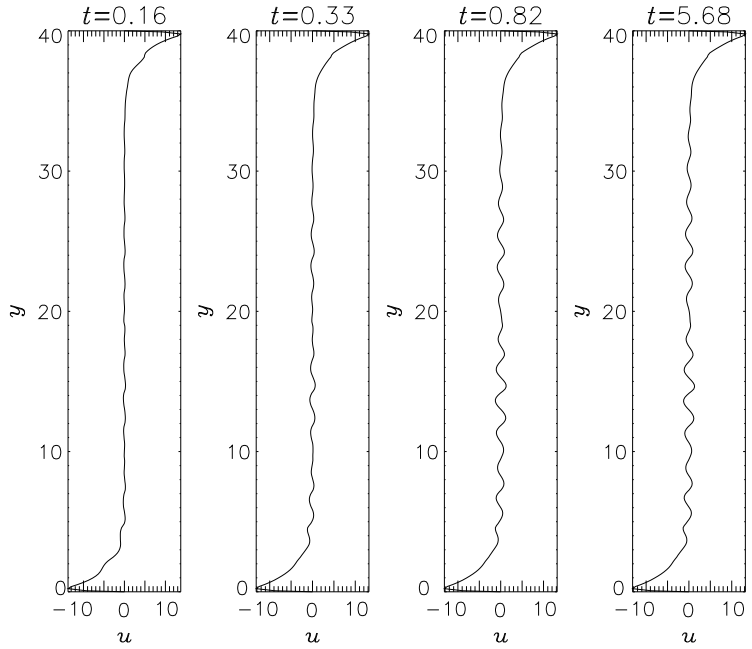


Fig. 15. Horizontal velocity at $x = 0.5$ for $\epsilon = 0.001$ and Gr $= 8170$.

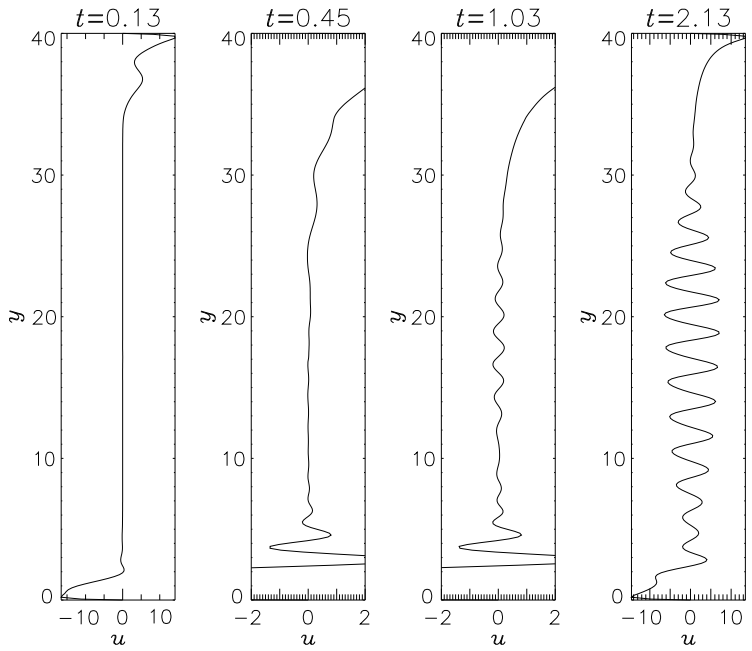


Fig. 16. Horizontal velocity component at $x = 0.5$ for $\epsilon = 0.3$ and Gr $= 9860$. Velocity range for $t = 0.45$ and $t = 1.03$ is made smaller to show the structure of the flow.

and $t = 2.13$. Strictly speaking, there exists a small difference between the critical Grashof numbers for linear and absolute instabilities for $\epsilon = 0.3$, but it is so small that the resolution of the numerical code was not sufficient to detect it. The disturbance wavenumber, which is estimated based on the average distance between the velocity peaks in the middle part of the last snapshot

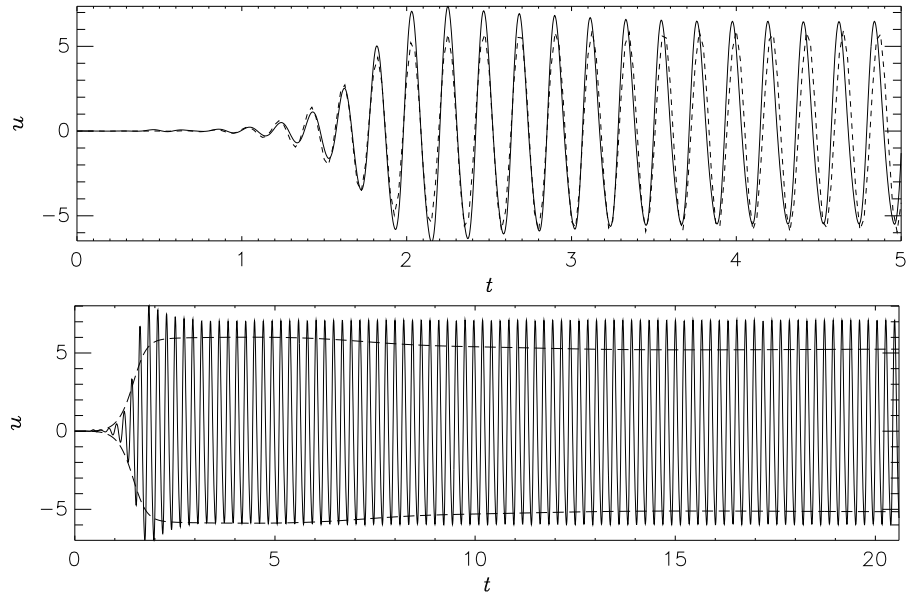


Fig. 17. Time history of the horizontal velocity component at the centre of the cavity at $\epsilon = 0.3$ and $\mathrm{Gr} = 9860$ for short (top) and long (bottom) time ranges. The dotted line in the top plot represents the CGLE velocity estimate for $u$; the dashed line in the bottom plot shows the CGLE estimate of the horizontal velocity amplitude.

in Fig. 16 is $\alpha \approx 2.75$ which agrees well with the value obtained from linear stability analysis (see Fig. 5 (b)).

In order to demonstrate the quantitative accuracy of the model we compare the time evolution of the CGLE solution with that obtained from DNS at the centre of the cavity $(x, y) = (0.5, 20)$. The most straightforward comparison is obtained for $u(0.5, 20, t)$ since the undisturbed flow at this location has zero horizontal velocity. Sample values from the DNS are compared with the values of the leading terms in the approximate solution given by (see Appendix A)

$$A(t, 20)u_{11}(0.5)E(20) + c.c.\,,$$

where $u_{11}$ is the horizontal velocity component of the eigenvector of the linearised problem and $A(t, 20)$ is given by the solution of equation (1) at $y = 20$. The choice of physical parameters for comparison between the DNS and model results is a delicate issue. The model is most accurate near the threshold of instability. In contrast, because of the limited resolution of the DNS code, its predictions of instability characteristics near criticality are least accurate: the disturbance amplitude is very small and the DNS stability results are the most vulnerable with respect to discretisation errors. On the other hand, further away from the critical point, where the accuracy of the DNS instability results improves, the model predictions become less accurate due to the increased range of nonlinear effects which it does not account for. Typically, monochromatic amplitude models in far supercritical regimes under-predict the saturation amplitude and over-predict the saturation time scale. The set

of physical parameters chosen for comparison of results is a compromise between these two conflicting influences. While the current model predictions are not completely free from the above deficiencies, Fig. 17 demonstrates remarkable agreement between the DNS and model results. The model is capable of capturing very fine detail of the temporal evolution of the flow. In order to match the phases between the DNS and CGLE results, when solving the CGLE the initial disturbance pulses were located at $y \approx 0.2$ and $y = 38.8$ at time $t = -0.35$. This is an empirical choice since the exact correspondence between the disturbances caused by the turning nonparallel flow near the ends of the cavity and the initial conditions for the CGLE is not known. The amplification rate up to time $t = 1.5$ was estimated assuming exponential growth obtained from the average over several oscillations of the quantity

$$\tilde{\sigma}^R = \frac{1}{t_{m,i+1} - t_{m,i}} \ln\left(\frac{u_{m,i+1}}{u_{m,i}}\right) ,$$

where $u_m$ is the local maximum of the horizontal velocity observed at time $t_m$ and $t_{m,i+1} - t_{m,i}$ is the approximate period of oscillations (see top plot in Fig. 17), $i$ and $i+1$ denoting two consecutive maxima. We find that $\tilde{\sigma}^R \approx 4$ which is larger than the amplification rate for the most amplified plane wave predicted by a linear stability analysis (which is 3.03). This is expected because in this situation the growth rate is determined not only by the linear amplification, but also by the propagating finite amplitude front of the localised disturbance wave envelope. The frequency of oscillations is estimated by averaging over a few oscillations the quantity

$$\tilde{\sigma}^I = \frac{2\pi}{t_{m,i+1} - t_{m,i}} .$$

The approximate frequency is found to be $\tilde{\sigma}^I \approx 32.8$ which agrees very well with the linear stability results of 32.5. For large times this value decreases to $\tilde{\sigma}^I \approx 29.0$. As shown by Suslov and Paolucci (1997b), the frequency of a weakly nonlinear state corresponding to a plane wave with an equilibrium amplitude $|A_e| = \sqrt{-\sigma^R / K_1^R}$ is $\hat{\sigma}^I = \sigma^I + K_1^I |A_e|^2$. This formula gives an estimate of $\hat{\sigma} \approx 28.8$ which is in excellent agreement with the observed value of $\tilde{\sigma}^I$ for large times as well. Finally, note a slight bias of the DNS results towards positive values of $u$ in the bottom plot of Fig. 17. This is consistent with Fig. 5(a) in Suslov and Paolucci (1997b) which shows that the weakly nonlinear self-interaction of the disturbance wave produces a mean flow which has positive horizontal velocity component near $x = 0.5$ whose magnitude is proportional to $|A|^2$. It is not accounted for by the first order disturbance envelope approximation shown by the dashed lines in the bottom plot of Fig. 17 which are symmetric with respect to the $u = 0$ level. Although not shown here, similar bias are found at other $y$-locations along the $x = 0.5$ plane. Finally note that after the initial rapid increase the amplitude predicted by CGLE decreases towards its saturated level achieved at $t \approx 14$. This initial overshoot with

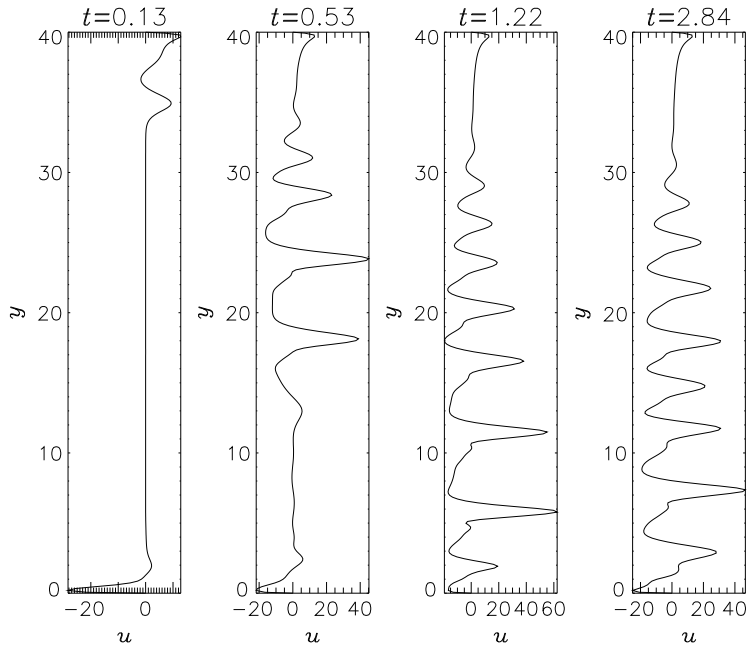


Fig. 18. Horizontal velocity component at $x = 0.5$ for $\epsilon = 0.6$ and $\mathrm{Gr} = 9860$.

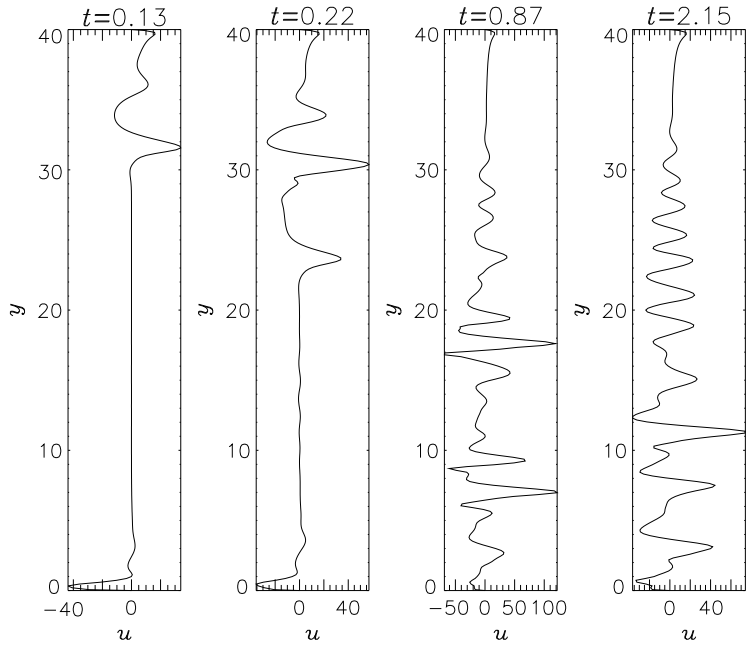


Fig. 19. Horizontal velocity component at $x = 0.5$ for $\epsilon = 0.6$ and $\mathrm{Gr} = 16900$.

subsequent relaxation is a consequence of the solitary structure seen in Fig. 9 and propagating with small negative group speed downwards. Such a long-living solitary structure is a result of the adopted impulse initial conditions and is a fully nonlinear solution of CGLE. It does not seem to be present in the DNS simulations with fully physically consistent initial conditions.

The flow arising in the strongly non-Boussinesq regime with $\epsilon = 0.6$ is much

more complicated than flows arising from moderate temperature differences between the walls. This complexity is two-fold. As can seen from Fig. 5 (c), both shear and buoyancy instability modes are present in general, and secondly, as shown by Suslov and Paolucci (1997b), the shear mode bifurcates subcritically. In such a situation the cubic CGLE may become inadequate since its solution becomes unbounded for sufficiently large initial conditions and at least a fifth order CGLE is necessary to obtain a bounded nonlinear state. Nevertheless meaningful qualitative conclusions can still be drawn from such a model.

When two interacting nonlinear modes define the flow pattern, two CGLEs modelling individual modes become coupled and lead to the following system of complex equations

$$\frac{\partial A_1}{\partial t} + c_{g1}\frac{\partial A_1}{\partial y} = (\sigma_1 + \lambda_1 K_{12})A_1 + M_1\frac{\partial^2 A_1}{\partial y^2} + K_{11}A_1|A_1|^2\,, \tag{26}$$

$$\frac{\partial A_2}{\partial t} + c_{g2}\frac{\partial A_2}{\partial y} = (\sigma_2 + \lambda_2 K_{21})A_2 + M_2\frac{\partial^2 A_2}{\partial y^2} + K_{22}A_2|A_2|^2\,, \tag{27}$$

$$\lambda_{1,2} = \frac{1}{A_H}\int_0^{A_H} |A_{2,1}|^2\,\mathrm{d}y\,, \tag{28}$$

as derived in Appendix E. This system of equations models global nonlinear coupling between two wave envelopes propagating with different group speeds (Knobloch and De Luca, 1990; Pierce and Wayne, 1995).

For $\mathrm{Gr} = 9860$ we obtain $\sigma_1 \approx (0.45, 77.5)$, $c_{g1} \approx -50.0$, $K_{11} \approx (-76.0, -150.6)$ and $M_1 \approx (14.7, 5.66)$. These coefficients are evaluated at $\alpha_{A_1} \approx 1.155$ and correspond to the buoyancy driven instability mode. For the shear driven mode at $\alpha_{A_2} \approx 2.815$ we obtain $\sigma_2 \approx (-23.1, 62.1)$, $c_{g2} \approx -7.28$, $K_{22} \approx (1.77 \times 10^4, 3.54 \times 10^4)$ and $M_2 \approx (16.8, -1.69)$. The coupling coefficients are $K_{12} \approx (-2.58 \times 10^4, 1.73 \times 10^4)$ and $K_{21} \approx (108.5, 3.47)$. Estimates of the two frequencies from the DNS results give $\tilde{\sigma}_1^I = 73.7$ and $\tilde{\sigma}_2^I = 63.2$ both agreeing fairly well with the linear analysis values. Based on the above numerical data, the following conclusions can be made. The flow in this regime is linearly convectively unstable with respect to buoyancy disturbances and stable with respect to shear disturbances. The buoyancy driven instability results from supercritical bifurcation while the shear driven disturbances destabilise the flow only if their initial amplitude is sufficiently large, as the corresponding bifurcation is subcritical. Both types of disturbances propagate downwards. Part of the buoyancy disturbance energy is transferred to the shear mode through nonlinear coupling ($K_{12}^R < 0$, $K_{21}^R > 0$). The numerical solution of the coupled CGLE's (not shown) confirms the convective nature of both disturbances: wave envelopes generated by the initial pulse at $y = \tilde{y}$ decay quickly as they propagate towards the bottom wall. The wave envelopes generated by

the initial pulse at $y = A_H - \tilde{y}$ also propagate downwards. Since the wave group speeds corresponding to the buoyancy and shear disturbances are substantially different, the two wave packets interact only for a limited time. For small amplitude initial pulses, the solution corresponding to the shear mode decays quickly as its linear amplification rate is negative, but larger initial amplitudes eventually blow-up (representing shear instability subcritically triggered and initially supported by the buoyant instability). As noted above, at least a quintic CGLE model is required to eliminate this singular behaviour. The buoyancy mode, while linearly unstable, dies out as soon as it reaches the bottom wall due to its convective nature and the zero boundary conditions. Mode coupling does not support its existence either because as discussed above the shear instability extracts energy from the buoyancy mode.

Snapshots of the DNS results for this regime are presented in Figs. 13 and 18. The parallel basic flow is established in the middle part of the cavity by time $t = 0.13$. Simultaneously a large amplitude disturbance is generated near the upper end of the cavity which propagates quickly downwards. This is the buoyancy disturbance: it is seen from the second snapshot in Fig. 13 that relatively large lumps of cold and more dense fluid with wavenumber $\alpha = \alpha_1 \approx 1.16$ move down the right (colder) wall. The amplitude of these buoyancy driven disturbances is so large that it triggers the subcritical transition to shear instability which is characterised by a wavelength of approximately half the size of that of the buoyancy disturbance, as seen in the snapshots at $t = 1.22$ and $t = 2.84$. Note that subcritical shear disturbances occupy a large part of the enclosure. This is not expected for a convective instability regime and indicates the presence of a nonlinear absolute instability which may exist for subcritically bifurcating flows as discussed in Couairon and Chomaz (1997). To show rigorously that the nonlinear absolute instability of the shear driven mode is indeed observed, one would need to analyse at least a fifth order CGLE, the derivation of which is beyond the scope of the current work.

An even more complicated flow is observed at the larger value of $\mathrm{Gr} = 16900$. In this case the buoyancy mode constants at $\alpha_{A_1} \approx 0.857$ are found to be $\sigma_1 \approx (3.57, 95.8)$, $c_{g1} \approx -87.3$, $K_{11} \approx (-74.7, -359.5)$ and $M_1 \approx (28.8, 9.42)$ and the shear mode constants evaluated at $\alpha_{A_2} \approx 2.580$ are $\sigma_2 \approx (4.52, 111.5)$, $c_{g2} \approx -20.3$, $K_{22} \approx (1.02 \times 10^3, -6.58 \times 10^3)$ and $M_2 \approx (22.1, -1.59)$. The mode coupling coefficients are $K_{12} \approx (-1.02 \times 10^4, 8.52 \times 10^3)$ and $K_{21} \approx (59.3, 532.1)$. Both modes are linearly convectively unstable and propagate downwards with the shear mode forming an irregular pattern at large times. The numerical solution of the coupled equations (26)–(27) presented in the first four snapshots in Fig. 10 has characteristics very similar to the ones described for the lower value of the Grashof number. Convectively unstable wave envelopes of buoyancy and shear disturbances interact only for a short time since they have very different group speeds and propagate in

a finite domain bounded by the absorbing walls (see snapshot for $t = 0.04$ and $t = 0.20$). Thus despite the global nature of coupling between equations (26)–(27) the interaction between these envelopes remains essentially local and is mostly limited to the short period of time when the localised envelopes share the same location in space. The wave envelopes induced by the initial pulses near the bottom of the cavity and seen for $t = 0.4$ at $y \sim \tilde{y}$ remain there as they are swept towards that wall with their negative group speed. Because of the convective character of instability the extension rate of these wave packets is not sufficiently large to overcome their drift and they decay quickly due to the absorbing influence of the nearby wall, see snapshot at $t = 0.20$. They are not seen at $t = 0.32$. The wave envelopes induced near the top of the cavity propagate downwards and spread but never occupy the whole cavity as they are only convectively unstable (see snapshots at $t = 0.20$ and 0.32). The wave envelopes corresponding to the buoyancy and shear modes are clearly distinguished for $t = 0.20$ and 0.32 by very different wavelengths. The buoyancy disturbance envelope moves faster and decays after it reaches $y = 0$ emphasising the convective nature of this instability and zero boundary conditions (compare snapshots for $t = 0.32$ and 0.68). The long term behaviour of the shear mode amplitude is essentially different. The initial envelope breaks into several parts and loses its symmetry as it hits $y = 0$: the wave amplitude is generally larger near $y = 0$ towards which the envelope propagates. The shear disturbance amplitude tends to zero near $y = A_H$ once again demonstrating the linearly convective character of instability of this mode. Nevertheless unlike the buoyancy mode the shear disturbances never decay even after reaching the bottom wall. This is because of the subcritical nature of the corresponding bifurcation ($K_{22}^R > 0$): by the time the shear envelope reaches the bottom of the cavity it has a magnitude larger than a threshold value of $A_{th} = \sqrt{\sigma_2^R / K_{22}^R} \approx 0.067$ so that the nonlinear destabilisation becomes sufficiently strong to maintain shear instability. The large amplitude subcritical shear disturbances existing in the lower part of the cavity may also trigger a nonlinear absolute instability (Couairon and Chomaz, 1997) which can result in a nonlinear global shear mode. The results seen in Fig. 10 at large times strongly indicate that this is the case, but no detailed investigation of this possibility has been performed as this would require incorporation of quintic nonlinear terms in the amplitude equations. Note that although the nonlinear cubic term in (27) plays a destabilising role, the solution remains bounded. This is partly due to the zero boundary conditions and partly due to the strong dissipation ($M_2^R > 0$). In addition, as discussed by Aranson and Kramer (2002), and references therein, the so-called phase gradient mechanism arrests the blow up of the subcritical pulse-like solution whenever $\left| M_2^I / K_{22}^I \right| \ll 1$ as indeed is the case in the problem considered.

The corresponding DNS results are presented in Figs. 14 and 19. After the parallel basic flow is established in the middle part of the cavity by time $t = 0.13$, the large buoyancy disturbance starts propagating from the top end of

the cavity. Its wavenumber is approximately 0.96 which is slightly larger than $\alpha_{A_1} \approx 0.857$ predicted by linear analysis. Since the $\sigma_2^R > 0$, the flow is linearly unstable with respect to shear disturbances. Indeed, the snapshot at $t = 0.22$ in Fig. 19 confirms this: the shear instability disturbances start developing in the lower part of the cavity, their estimated wavenumber is approximately 2.50 which is reasonably close to $\alpha_{A_2} \approx 2.580$. The two instability modes interact at larger times resulting in a somewhat irregular flow pattern ($t = 0.87$). Eventually, the convectively unstable buoyancy disturbance reaches the bottom wall and decays while the slower propagating shear disturbances form the pattern seen in the upper part of the snapshot at $t = 2.15$. This snapshot agrees qualitatively with the numerical solution of CGLE shown in the top plot in Fig. 10: regular periodic tail and irregular head of the resulting wave envelope. The DNS results for larger times (not presented) show that the buoyancy disturbance is generated again and the qualitative flow scenario described above is repeated.

For larger values of the Grashof number the shear instability becomes absolute and the numerical solution of the corresponding CGLE does not decay near $y = A_H$. The DNS results show irregular flow patterns in the cavity in these regimes.

We note that flow patterns observed in DNS for the larger Grashof numbers reveal fast velocity variations along the cavity (see Fig. 19). They are primarily caused by the buoyancy mode disturbances which have much smaller critical Grashof number than the shear ones. Because of the large supercriticality for the buoyancy disturbances in such regimes they are unlikely to remain two-dimensional. In contrast the shear mode is still predominantly two-dimensional due to the lower degree of its supercriticality. Indeed the last snapshots in Figs 14 and 19 show that once the fast moving large amplitude buoyancy envelope propagates away (confirming that its nature remains convective as discussed in Section 5.1) it leaves behind a pattern typical for two-dimensional shear disturbances predicted by the analysis. Thus the character of instability is still expected to be reasonably accurately determined through the two-dimensional analysis. Two additional reasons can be given to advocate this. First, in the present work we are specifically interested in transition between *linear* absolute and convective instabilities in the longitudinal direction. Even if nontrivial dynamics exists in the transverse direction it is linearly fully decoupled from that of interest and the two-dimensional study is sufficient for our purpose. Second, although in the centre of the buoyancy wave envelope the disturbances are sufficiently large and could become three-dimensional, the character of linear instability is fully determined by the relative motion of the edges of the wave envelopes. There the disturbance amplitudes are small by definition and standard linear analysis is applicable which shows that two-dimensional disturbances are the most dangerous, see the discussion in the beginning of Section 3 and results reported in Suslov and Paolucci (1995a).

Nevertheless, it is clear that extending the present analysis to the quintic CGLE, in conjunction with a three-dimensional DNS study, can enhance our understanding of this interesting and relevant flow.

## 6 Conclusions

Non-Boussinesq regimes with large fluid property variations reveal a rich variety of possible flow patterns in very simple geometries. A systematic procedure of deriving the complex Ginzburg-Landau model of near critical flows is presented for such cases. Analysis of its infinitesimal solutions shows various spatio-temporal scenarios corresponding to convective and absolute instabilities of the basic parallel flow. Special attention is paid to the aspects of physical relevance and accuracy of the developed Ginzburg-Landau model when it is used to determine the transition between absolute and convective instabilities. It is shown that the CGLE based predictions of the transition can be accurate only if the full physical dispersion relation is close to a quadratic function over the complete range of disturbance wavenumbers with positive linear amplification rate. In this case the coefficients of the CGLE can be evaluated at any wavenumber in the parabolic range of the physical dispersion relation. Such models result in identical long term behaviours due to the wavenumber cascading towards that of the most amplified disturbance. These criteria are formulated as simple accuracy tests which are shown to be satisfied in the problem of natural convection in a tall vertical enclosure. In applying the model to the non-Boussinesq convection flow, we show that fluid property variations in the vertical differentially-heated cavity have a strong influence on the character of flow bifurcations. In particular, as the temperature difference between the walls of the enclosure increases, the shear driven bifurcation changes character from supercritical to subcritical, and the corresponding instability changes from absolute to convective. It becomes absolute again only if the Grashof number is increased to a finite value above the linearly critical one. At very large temperature differences, a buoyancy driven instability mode appears as a result of a supercritical bifurcation. This instability is found to be of convective type for the complete range of Grashof numbers investigated. These conclusions are based solely on the analysis of the complex Ginzburg-Landau equations derived for the flow, but are confirmed by DNS results of the corresponding two-dimensional flows. Remarkably, although the presented theory of CGLEs is developed for an effectively infinite geometry, and as such does not account rigorously for details of the distant top and bottom boundary conditions, the results are in excellent agreement with those of the DNS in a finite cavity of aspect ratio 40. This confirms the validity of our qualitative arguments regarding the weak boundary condition influence when the symmetry $y \to -y$ is broken.

Experiments in the weakly non-Boussinesq regime (Simpkins, 1989) also confirm the two-dimensionality of the instability and provide quantitative evidence of the accuracy of critical parameters (Simpkins, 1993). More recent high pressure convection experiments in an inclined enclosure of large aspect ratio (Daniels, Plapp, and Bodenschatz, 2000) confirm the qualitative symmetry-breaking influence of the non-Boussinesq fluid property variations on spatio-temporal instability of convection resulting in the preferred downward disturbance propagation and convective instability. Unfortunately, no quantitative information on such flows has been reported to date. This is partly due to technical difficulties associated with measuring flow characteristics under high pressure/temperature conditions. For this reason, theoretical analysis in conjunction with numerical simulations still remain the only tools for investigating the physics of non-Boussinesq flows.

While our analytical results are in excellent agreement with those obtained by numerical simulations, thus demonstrating the accuracy of the model developed, we hope that our work will motivate future experimental research in this area as it is shown to provide an even richer variety of flow patterns than the well studied classical Rayleigh-Bénard and Taylor-Couette flows. As noted by Moresco and Healey (2000), although complex convection flows are found in various practical applications, reports of their experimental investigation are still surprisingly rare.

## A Multiple scale expansions

We look for the solution of problem (2)–(11) in the separable Fourier-decomposed form

$$\boldsymbol{W}(t,x,y) = \sum_{m=0}^{\infty} \sum_{n=-\infty}^{\infty} \varepsilon^m A_{mn} \boldsymbol{w}_{mn} E^n \,, \tag{A.1}$$

where $\boldsymbol{w}_{mn} = (u_{mn}(x), v_{mn}(x), T_{mn}(x), \Pi_{mn}(x) + \delta_{0n}\Pi_{m0}y)^{\mathrm{T}}$, $E = \exp(\mathrm{i}\alpha y)$ is a Fourier component of the disturbance corresponding to wavenumber $\alpha$, and $0 < \varepsilon \ll 1$ is a small parameter representing the size of the time-dependent disturbance amplitude which is allowed to vary slowly in $y$. The terms $\Pi_{m0}y$ in the expansion for the dynamic pressure are necessary in order to take into account the constant vertical pressure gradient required to maintain a zero average mass flux through any horizontal cross-section when disturbances are developing. The expansion for the spatially uniform thermodynamic pressure $P$ is

$$P = \sum_{m=0}^{\infty} \varepsilon^m A_{m0} P_{m0} \,, \tag{A.2}$$

where the individual (constant) terms $P_{m0}$ are determined at each order from the global mass conservation condition (9). We also introduce the property

vector $\boldsymbol{g} = (\rho, c_p, \mu, k)^{\mathrm{T}}$, which is expanded similarly to (A.1):

$$\boldsymbol{g}(t,x,y) = \sum_{m=0}^{\infty} \sum_{n=-\infty}^{\infty} \varepsilon^m A_{mn} \boldsymbol{g}_{mn} E^n \,, \tag{A.3}$$

where, in particular,

$$\begin{aligned}
&\boldsymbol{g}_{11} = \boldsymbol{g}_{00T} T_{11} \,, \quad \boldsymbol{g}_{20} = \boldsymbol{g}_{00T} T_{20} + \boldsymbol{g}_{00TT} |T_{11}|^2 + \boldsymbol{g}_{00P} P_{20} \,, \\
&\boldsymbol{g}_{21} = \boldsymbol{g}_{00T} T_{21} \,, \quad \boldsymbol{g}_{22} = \boldsymbol{g}_{00T} T_{22} + \frac{1}{2} \boldsymbol{g}_{00TT} T_{11}^2 \,, \\
&\boldsymbol{g}_{31} = \boldsymbol{g}_{00T} T_{31} + \boldsymbol{g}_{00TT} (T_{11} T_{20} + T_{11}^* T_{22}) + \frac{1}{2} \boldsymbol{g}_{00TTT} T_{11} |T_{11}|^2 \\
&\qquad + \boldsymbol{g}_{00TP} T_{11} P_{20} \,,
\end{aligned} \tag{A.4}$$

the subscripts $T$ and $P$ denote partial differentiation with respect to $T_{00}(x)$ and $P_{00}$ of the equation of state or corresponding property variation formulae, and the star superscript denotes complex conjugation. Now we assume the existence of multiple time and spatial scales so that $A_{mn}(t,y) = A_{mn}(t_0, t_1, t_2, \ldots, y_1, y_2, \ldots)$, where we take $t_0 = t,\ t_1 = \varepsilon t,\ t_2 = \varepsilon^2 t, \ldots$ and $y_0 = y,\ y_1 = \varepsilon y,\ y_2 = \varepsilon^2 y, \ldots$ so that

$$\begin{aligned}
\frac{\partial}{\partial t} &= \frac{\partial}{\partial t_0} + \varepsilon \frac{\partial}{\partial t_1} + \varepsilon^2 \frac{\partial}{\partial t_2} + \cdots \,, \\
\frac{\partial}{\partial y} &= \frac{\partial}{\partial y_0} + \varepsilon \frac{\partial}{\partial y_1} + \varepsilon^2 \frac{\partial}{\partial y_2} + \cdots \,.
\end{aligned} \tag{A.5}$$

The amplitudes $A_{mn}$, being functions of "long" spatial scales at which the modulation of a fundamental harmonic can be observed, do not depend on $y_0$ since the periodicity of the disturbance is taken into account explicitly by the exponentials $E^n(y_0)$.

Substituting expansions (A.1) and (A.3) into system (2)–(11), we obtain a set of equations at each order of $\varepsilon$ and $E$. Since the equations for $E^n$ and $E^{-n}$ are complex conjugates of each other, we limit our consideration to the equations for positive values of $n$. Note that $w_{mn}^* = w_{m-n}$, $A_{mn}^* = A_{m-n}$, $A_{00} = 1$, $A_{0n\neq 0} = A_{1|n|\neq 1} = 0$ (for details see Suslov and Paolucci (1997b)). The specific form of the equations at each order will define the functional form of the dependence of higher-order amplitudes $A_{mn}$ on $A_{11}$ as demonstrated next.

## B Linearised disturbances

At order $\varepsilon^1 E^1$ we obtain the linear perturbation equations, which upon making the identification $A \equiv A_{11}$, can be given in matrix form as

$$\left( A\mathsf{A}_\alpha - \frac{\partial A}{\partial t_0}\mathsf{B} \right) \boldsymbol{w}_{11} = 0\,, \tag{B.1}$$

where $\boldsymbol{w}_{11} = (u_{11}, v_{11}, T_{11}, \Pi_{11})^{\mathrm{T}}$, $u_{11} = v_{11} = T_{11} = 0$ at $x = 0, 1$, and the elements of $\mathsf{A}_\alpha$ and $\mathsf{B}$ are given in Suslov and Paolucci (1997b). This system of linear differential equations has a nontrivial solution of the form $A\boldsymbol{w}_{11}$, where $A = \tilde{A}(t_1, t_2, \ldots, y_1, y_2, \ldots)\mathrm{e}^{\sigma t_0}$ only if operator on the left hand side of the equation is singular and $\sigma = \sigma^R + \mathrm{i}\sigma^I$ and $\boldsymbol{w}_{11}$ are respectively the eigenvalues and eigenvectors of the generalised eigenvalue problem

$$(\mathsf{A}_\alpha - \sigma\mathsf{B})\boldsymbol{w}_{11} = 0\,. \tag{B.2}$$

This problem has been solved for a wide range of $\epsilon$ and Gr in Suslov and Paolucci (1995b). The eigenvectors are normalised in such a way that

$$\max|v_{11}| = \max|v_{00}|\,,$$

so we can judge the disturbance magnitude by its amplitude only.

The system (B.2), with discretised spatial variable, reduces to an algebraic eigenvalue problem. For future convenience we define the corresponding discrete singular matrix operator $\mathsf{L}_{\alpha,\sigma} \equiv \mathsf{A}_\alpha - \sigma\mathsf{B}$ and its adjoint $\mathsf{L}^\dagger_{\alpha,\sigma} \equiv (\mathsf{A}^*_\alpha - \sigma^*\mathsf{B}^*)^{\mathrm{T}}$ such that

$$\mathsf{L}^\dagger_{\alpha,\sigma}\boldsymbol{w}^\dagger_{11} = 0\,, \tag{B.3}$$

where $\boldsymbol{w}^\dagger_{11}$ is the discrete adjoint eigenvector normalised in such a way that

$$\left\langle \boldsymbol{w}^\dagger_{11}, \mathsf{B}\boldsymbol{w}_{11} \right\rangle = 1. \tag{B.4}$$

The inner product of two discrete $N$-component vectors $\boldsymbol{a}$ and $\boldsymbol{b}$, denoted by angle brackets, is defined as $\langle \boldsymbol{a}, \boldsymbol{b} \rangle \equiv \sum_{i=1}^{N} a_i^* b_i$. Subsequently, from (B.2) and (B.4) follows the dispersion relation

$$\sigma = \left\langle \boldsymbol{w}^\dagger_{11}, \mathsf{A}_\alpha \boldsymbol{w}_{11} \right\rangle\,. \tag{B.5}$$

Differentiating (B.2) with respect to $\alpha$ we obtain

$$\mathsf{L}_{\alpha,\sigma}\frac{\partial \boldsymbol{w}_{11}}{\partial \alpha} = -\frac{\partial \mathsf{L}_{\alpha,\sigma}}{\partial \alpha}\boldsymbol{w}_{11} = -\left( \frac{\partial \mathsf{A}_\alpha}{\partial \alpha} - \frac{\partial \sigma}{\partial \alpha}\mathsf{B} \right) \boldsymbol{w}_{11} \tag{B.6}$$

and

$$\mathsf{L}_{\alpha,\sigma}\frac{\partial^2 \boldsymbol{w}_{11}}{\partial \alpha^2} = -\left( \frac{\partial^2 \mathsf{L}_{\alpha,\sigma}}{\partial \alpha^2}\boldsymbol{w}_{11} + 2\frac{\partial \mathsf{L}_{\alpha,\sigma}}{\partial \alpha}\frac{\partial \boldsymbol{w}_{11}}{\partial \alpha} \right)\,. \tag{B.7}$$

Then, considering the inner products of $\boldsymbol{w}_{11}^{\dagger}$ with (B.6), and using (B.3) and (B.4), we obtain

$$\frac{\partial\sigma}{\partial\alpha} = -\mathrm{i}\frac{\partial\omega}{\partial\alpha} = -\mathrm{i}c_g = \left\langle \boldsymbol{w}_{11}^{\dagger}, \frac{\partial \mathsf{A}_\alpha}{\partial\alpha}\boldsymbol{w}_{11} \right\rangle , \tag{B.8}$$

where $\omega \equiv \mathrm{i}\sigma$ is the complex frequency and $c_g = c_g^R + \mathrm{i}c_g^I$ is the complex group speed of the packet of disturbance waves centred at wavenumber $\alpha$. Note that the group speed defined by (B.8) is real only at values of $\alpha$ providing maximum or minimum linear amplification rates, i.e. along lines $A$ and $B$ in Fig. 1 (a), since for these wavenumbers $c_g^I = \partial\sigma^R/\partial\alpha = 0$. For all other values of $\alpha$, $c_g^I \neq 0$ (see Craik, 1985, page 14). From (B.7) we also obtain

$$\frac{\partial^2\sigma}{\partial\alpha^2} = \left\langle \boldsymbol{w}_{11}^{\dagger}, 2\frac{\partial \mathsf{L}_{\alpha,\sigma}}{\partial\alpha}\frac{\partial\boldsymbol{w}_{11}}{\partial\alpha} + \frac{\partial^2 \mathsf{A}_\alpha}{\partial\alpha^2}\boldsymbol{w}_{11} \right\rangle , \tag{B.9}$$

which will be used in Appendix D.

## C Second order terms

Collecting terms at order $\varepsilon^2 E^1$ we have

$$\left(A_{21}\mathsf{A}_\alpha - \frac{\partial A_{21}}{\partial t_0}\mathsf{B}\right)\boldsymbol{w}_{21} = \left(\mathrm{i}\frac{\partial A}{\partial y_1}\frac{\partial \mathsf{A}_\alpha}{\partial\alpha} + \frac{\partial A}{\partial t_1}\mathsf{B}\right)\boldsymbol{w}_{11}\,, \tag{C.1}$$

where $\boldsymbol{w}_{21} = (u_{21}, v_{21}, T_{21}, \Pi_{21})^{\mathrm{T}}$ and $u_{21} = v_{21} = T_{21} = 0$ at $x = 0, 1$. Since, as shown in Appendix B, $A \sim \mathrm{e}^{\sigma t_0}$, compatibility of the left- and right-hand sides of (C.1) requires that $A_{21} = \tilde{A}_{21}(t_1, t_2, \ldots, y_1, y_2, \ldots)\mathrm{e}^{\sigma t_0}$ so that $\partial A_{21}/\partial t_0 = \sigma A_{21}$. Then upon using (B.4) and (B.8) the inner product between equation (C.1) and the solution $\boldsymbol{w}_{11}^{\dagger}$ of the adjoint problem results in

$$0 = c_g\frac{\partial A}{\partial y_1} + \frac{\partial A}{\partial t_1}\,, \tag{C.2}$$

i.e. the disturbance amplitude $A = \tilde{A}(Y_1, t_2, y_2, \ldots)\,\mathrm{e}^{\sigma t_0}$, $Y_1 = y_1 - c_g t_1$. Then problem (C.1) is transformed to

$$A_{21}\mathsf{L}_{\alpha,\sigma}\boldsymbol{w}_{21} = \frac{\partial A}{\partial Y_1}\left(\mathrm{i}\frac{\partial \mathsf{A}_\alpha}{\partial\alpha} - c_g\mathsf{B}\right)\boldsymbol{w}_{11}\,. \tag{C.3}$$

It is clear now that compatibility of the left- and right-hand sides requires $A_{21} = \partial A/\partial Y_1$.

Solvability condition (C.2) puts the right-hand side of equation (C.1) in the range of the singular linear operator $\mathsf{L}_{\alpha,\sigma}$ so that equation (C.1) has infinitely

many solutions. Indeed by comparing (C.3) and (B.6), we see that the multitude of solution of (C.3) can be written as

$$\boldsymbol{w}_{21} = -\mathrm{i}\frac{\partial \boldsymbol{w}_{11}}{\partial \alpha} + r\boldsymbol{w}_{11}\,, \tag{C.4}$$

where $r$ is an arbitrary constant. To eliminate this ambiguity we impose an extra orthogonality condition $\langle \boldsymbol{w}_{mn}, \boldsymbol{w}_{11}\rangle = 0$ when $m \neq 1$ or $n \neq 1$. Physically this means that the disturbance amplitude $A$ is chosen in such a way that the higher order corrections to the solution do not affect the intensity of the component of the complete solution given by the eigenfunctions $\boldsymbol{w}_{11}$ and only add orthogonal modifications. Requiring $\langle \boldsymbol{w}_{21}, \boldsymbol{w}_{11}\rangle = 0$ fixes $r$ to the unique value

$$r = \mathrm{i}\frac{\langle \boldsymbol{w}_{11}, \partial \boldsymbol{w}_{11}/\partial\alpha\rangle}{\langle \boldsymbol{w}_{11}, \boldsymbol{w}_{11}\rangle}\,.$$

Equations for the mean flow correction arising from terms of the order $\varepsilon^2 E^0$ and for the second harmonic arising from terms of the order $\varepsilon^2 E^2$ have been obtained and discussed in detail in Suslov and Paolucci (1997b) and Suslov and Paolucci (1999) and are not repeated here. We only note that unless special resonant conditions occur (which does no happen in this study) (see Suslov and Paolucci, 1997b) the operators $\mathsf{L}_{0,2\sigma}$ and $\mathsf{L}_{2\alpha,2\sigma}$ are not singular and no issues of solvability or non-uniqueness have to be resolved at these orders.

## D Complex Ginzburg-Landau equation

The system which results at order $\varepsilon^3 E^1$ is given by

$$\begin{aligned}\left(A_{31}\mathsf{A}_\alpha - \frac{\partial A_{31}}{\partial t_0}\mathsf{B}\right)\boldsymbol{w}_{31} = A|A|^2\boldsymbol{f}_{31} + \frac{\partial^2 A}{\partial Y_1^2}\left(\mathrm{i}\frac{\partial \mathsf{A}_\alpha}{\partial\alpha}\boldsymbol{w}_{21} + \frac{1}{2}\frac{\partial^2 \mathsf{A}_\alpha}{\partial\alpha^2}\boldsymbol{w}_{11}\right)\\ + \mathrm{i}\frac{\partial A}{\partial y_2}\frac{\partial \mathsf{A}_\alpha}{\partial\alpha}\boldsymbol{w}_{11} + \mathsf{B}\left(\frac{\partial A}{\partial t_2}\boldsymbol{w}_{11} - c_g\frac{\partial^2 A}{\partial Y_1^2}\boldsymbol{w}_{21}\right)\,,\end{aligned} \tag{D.1}$$

where $\boldsymbol{w}_{31} = (u_{31}, v_{31}, T_{31}, \Pi_{31})^{\mathrm{T}}$, $u_{31} = v_{31} = T_{31} = 0$ at $x = 0, 1$, and we have taken into account that, as follows from (C.2),

$$\frac{\partial^2 A}{\partial t_1 \partial y_1} = -c_g\frac{\partial^2 A}{\partial y_1^2} = -c_g\frac{\partial^2 A}{\partial Y_1^2}\,.$$

The vector $\boldsymbol{f}_{31} = \left(f_{31}^{(1)}, f_{31}^{(2)}, f_{31}^{(3)}, f_{31}^{(4)}\right)^{\mathrm{T}}$ is a function of solutions obtained at lower orders of $\varepsilon$ and is given in Suslov (1997). The right-hand side of (D.1) consists of terms with three different functional dependencies on the amplitude $A$: $A|A|^2$, $\partial^2 A/\partial Y_1^2$, $\partial A/\partial y_2$. Therefore in order to guarantee the compatibility

of the system for different times it has to be split into three independent parts representing each of the above functional forms. This also requires the slow evolution of amplitude $A$ to depend in general on the same three functional forms, namely,

$$\frac{\partial A}{\partial t_2} = K_1 A|A|^2 + K_2 \frac{\partial^2 A}{\partial Y_1^2} + K_3 \frac{\partial A}{\partial y_2}\,.$$

Our goal now is to obtain the constants $K_1$, $K_2$ and $K_3$.

Equation (D.1) splits into a system of three equations

$$\left(A_{31}^{(1)}\mathsf{A}_\alpha - \frac{\partial A_{31}^{(1)}}{\partial t_0}\mathsf{B}\right)\boldsymbol{w}_{31}^{(1)} = A|A|^2\left(\boldsymbol{f}_{31} + K_1\mathsf{B}\boldsymbol{w}_{11}\right)\,, \tag{D.2}$$

$$\left(A_{31}^{(2)}\mathsf{A}_\alpha - \frac{\partial A_{31}^{(2)}}{\partial t_0}\mathsf{B}\right)\boldsymbol{w}_{31}^{(2)} = \frac{\partial^2 A}{\partial Y_1^2}\left[\left(\mathrm{i}\frac{\partial \mathsf{A}_\alpha}{\partial \alpha} - c_g\mathsf{B}\right)\boldsymbol{w}_{21} + \left(\frac{1}{2}\frac{\partial^2 \mathsf{A}_\alpha}{\partial \alpha^2} + K_2\mathsf{B}\right)\boldsymbol{w}_{11}\right]\,, \tag{D.3}$$

$$\left(A_{31}^{(3)}\mathsf{A}_\alpha - \frac{\partial A_{31}^{(3)}}{\partial t_0}\mathsf{B}\right)\boldsymbol{w}_{31}^{(3)} = \frac{\partial A}{\partial y_2}\left(\mathrm{i}\frac{\partial \mathsf{A}_\alpha}{\partial \alpha} + K_3\mathsf{B}\right)\boldsymbol{w}_{11}\,. \tag{D.4}$$

Now compatibility of the left- and right-hand sides requires $A_{31}^{(1)} = A|A|^2$, $A_{31}^{(2)} = \partial^2 A/\partial Y_1^2$, $A_{31}^{(3)} = \partial A/\partial y_2$ so that the above equations become

$$\mathsf{L}_{\alpha,\sigma+2\sigma^R}\boldsymbol{w}_{31}^{(1)} = \boldsymbol{f}_{31} + K_1\mathsf{B}\boldsymbol{w}_{11}\,, \tag{D.5}$$

$$\mathsf{L}_{\alpha,\sigma}\boldsymbol{w}_{31}^{(2)} = \left(\mathrm{i}\frac{\partial \mathsf{A}_\alpha}{\partial \alpha} - c_g\mathsf{B}\right)\boldsymbol{w}_{21} + \left(\frac{1}{2}\frac{\partial^2 \mathsf{A}_\alpha}{\partial \alpha^2} + K_2\mathsf{B}\right)\boldsymbol{w}_{11}\,, \tag{D.6}$$

$$\mathsf{L}_{\alpha,\sigma}\boldsymbol{w}_{31}^{(3)} = \left(\mathrm{i}\frac{\partial \mathsf{A}_\alpha}{\partial \alpha} + K_3\mathsf{B}\right)\boldsymbol{w}_{11}\,. \tag{D.7}$$

The linear operator on the left-hand side of equation (D.5) is typically not singular and therefore this equation has a unique solution for any value of $K_1$. Thus, orthogonality rather than the conventional solvability condition has to be used to fix the value of this constant. As shown in Suslov and Paolucci (1997b), the condition $\langle \boldsymbol{w}_{31}^{(1)}, \boldsymbol{w}_{11}\rangle = 0$ leads to

$$K_1 = -2\sigma^R\frac{\langle \boldsymbol{w}_{11}, \boldsymbol{\chi}\rangle}{\langle \boldsymbol{w}_{11}, \boldsymbol{w}_{11}\rangle}\,, \tag{D.8}$$

where $\boldsymbol{\chi} = (u_\chi, v_\chi, T_\chi, \Pi_\chi)^{\mathrm{T}}$ is the solution of

$$\mathsf{L}_{\alpha,\sigma+2\sigma^R}\boldsymbol{\chi} = \boldsymbol{f}_{31}\,.$$

Note that the above value of $K_1$ approaches the value given by the standard solvability condition in the limit $\sigma^R \to 0$.

Since the linear operators on the left-hand sides of equations (D.6) and (D.7) are singular we apply the solvability condition, i.e. consider the inner product of these equations with $\boldsymbol{w}_{11}^{\dagger}$. Then using (B.4)–(B.9) and (C.4) we obtain

$$K_2 = -\frac{1}{2}\frac{\partial^2 \sigma}{\partial \alpha^2}\,, \quad K_3 = -c_g\,. \tag{D.9}$$

Now reconstituting the time derivative of the amplitude, we have

$$\frac{\partial A}{\partial t_0} + \varepsilon\frac{\partial A}{\partial t_1} + \varepsilon^2\frac{\partial A}{\partial t_2} + \cdots = \sigma A - c_g\left(\varepsilon\frac{\partial A}{\partial y_1} + \varepsilon^2\frac{\partial A}{\partial y_2}\right) + \varepsilon^2 K_2\frac{\partial^2 A}{\partial y_1^2} + \varepsilon^2 K_1 A|A|^2 + \cdots\,,$$

or using (A.5)

$$\frac{\partial A}{\partial t} = \sigma A - c_g\frac{\partial A}{\partial y} + K_2\frac{\partial^2 A}{\partial y^2} + \varepsilon^2 K_1 A|A|^2 + \cdots\,.$$

Multiplying the above equation by $\varepsilon$, redefining $\varepsilon A \to A$ and neglecting the higher-order terms in amplitude we obtain the CGLE (1) for the amplitude $A = A(t, y)$ of a spatially modulated monochromatic disturbance.

We note two aspects which distinguish the above derivation from those conventionally found in the literature. First, the disturbance amplitude is allowed to be a function of the fast time $t_0$ and its magnitude is not directly related to the distance from criticality. This means that we do not impose the conventional requirements $|\sigma^R| = O(\varepsilon^2)$ and $(Gr - Gr_c)/Gr_c = O(\varepsilon^2)$ (see Herbert, 1983). They are avoided by using the orthogonality condition in addition to the solvability condition at various orders of small amplitude as was first suggested by the authors in Suslov and Paolucci (1997b). Naturally, this does not imply that the derived amplitude equation is valid arbitrarily far from criticality. Indeed the requirement of small amplitude is equivalent to $|A| \sim \sqrt{-\sigma^R/K_1^R} = O(\varepsilon) \ll 1$ which in turn defines the relation between the fast (linear) and slow (nonlinear) timescales. This condition is definitely satisfied near the criticality, but might fail far away from it. At the same time, in some physical problems, and in particular in the one considered here, it might hold farther away from criticality than a distance of order $\varepsilon^2$. This condition is checked a posteriori when the numerical values of the coefficients are computed and is found to be well satisfied in the current work. Second, the derivation presented here does not rely on the fact that $\alpha$ is the wavenumber corresponding to the largest linear amplification rate $\sigma^R$. Implications of this are very

delicate and are discussed in the body of the current paper. The main outcome of this extended treatment is the computationally straightforward and inexpensive criterion which is formulated in Section 4 and which allows one to *quantify* the bounds of critical parameters for transition between convective and absolute instabilities when using the CGLE as a working model.

## E Coupled equations for two-mode regimes

When linear stability analysis predicts the existence of two instability modes a system of coupled amplitude equations describes the dynamics. Assuming that two instability modes are present in the flow, each of which is characterised by its own amplitude $A_i = O(\varepsilon)$, wavenumber $\alpha_i$, complex linear amplification rate $\sigma_i$ and group speed $c_{gi}$, $i = 1, 2$, fully uncoupled sets of equations arise for each of the modes for the fast spatial variation given by $E_i$ up to and including terms of second order in $\varepsilon$. Coupling terms, of the form $A_1|A_2|^2$ and $A_2|A_1|^2$, appear at third order in $\varepsilon$. Using the same procedure as described in Appendix D, these extra terms lead to a separate system of equations

$$\left(A_{311}\mathsf{A}_{\alpha_1} - \frac{\partial A_{311}}{\partial t_0}\mathsf{B}\right)\boldsymbol{w}_{311} = A_1|A_2|^2\boldsymbol{f}_{311} + \frac{\partial A_1}{\partial t_2}\mathsf{B}\boldsymbol{w}_{111}\,, \qquad \text{(E.1)}$$

where the vector $\boldsymbol{f}_{331}$ depends on solutions obtained at lower orders in $\varepsilon$ and is defined in Suslov and Paolucci (1997a,b). Subsequently, the coupling amplitude has to be of the form $A_{311} = A_1|A_2|^2$ and the slow time derivative of $A_1$ has to be of a similar form, $\partial A_1/\partial t_2 = K_{12}A_1|A_2|^2$. As in Appendix D this results in an equation with a non-singular operator on the left-hand side

$$\mathsf{L}_{\alpha_1,\sigma_1+2\sigma_2^R}\boldsymbol{w}_{311}^{(1)} = (\boldsymbol{f}_{311} + K_{12}\mathsf{B}\boldsymbol{w}_{111})\,, \qquad \text{(E.2)}$$

where the constant $K_{12}$ is uniquely determined by the orthogonality condition (see equation (D.8)). Such a procedure leads to a system of two coupled Ginzburg-Landau equations

$$\frac{\partial A_i}{\partial t} + c_{gi}\frac{\partial A_i}{\partial y} = \sigma_i^R A_i + M_i\frac{\partial^2 A_i}{\partial y^2} + K_{i1}A_i|A_1|^2 + K_{i2}A_i|A_2|^2\,, \quad i = 1, 2\,. \qquad \text{(E.3)}$$

As discussed by Knobloch and De Luca (1990) and Pierce and Wayne (1995), this set of equations although mathematically correct may be incomplete as it only describes local wave interactions. Indeed the only interactions in this system are due to the cubic terms $A_i|A_{3-i}|^2$ which only contribute if the two wave envelopes are found at the same physical location at the same time. In the case of localised wave packets propagating with different group speeds, which is relevant to convective and absolute instabilities considered in this

work, this interaction time is small and, as discussed by Pierce and Wayne (1995), coupled CGLEs exclude the possibility of mutual spatial modulation of the two wave envelopes propagating with different group speeds. The numerical simulation of equations (E.3) conducted by the authors confirms this conclusion.

In order to account for nonlocal mode coupling, we generalise the procedure of Knobloch and De Luca (1990). Originally it was developed for counter-propagating waves with the same group speed. Here we consider the case of waves propagating with arbitrary group speeds. In order to accomplish this, we allow small perturbations $B_i$ of the fundamental amplitudes $A_i$. As shown in Appendix C, amplitudes $A_i$ are functions of $Y_{1i} = y_1 - c_{gi}t_1$. Thus the coupling amplitudes are chosen to be of the form $\varepsilon A_i(Y_{1i}, t_2, y_2, \ldots) + \varepsilon^2 B_i(Y_{1,3-i}, t_2, y_2, \ldots)$, $i = 1, 2$. The equations for $B_i$ resulting at second order in $\varepsilon$ are identical to the linearised equations (B.1). At order $\varepsilon^3$, amplitudes $B_i$ introduce terms proportional to $E^0$, $E_1$, $E_2$, $E_1^2$, $E_2^2$, $E_1^{-2}$, $E_2^{-2}$, $E_1E_2$, $E_1E_2^{-1}$, $E_1^{-1}E_2$, and $E_1^{-1}E_2^{-1}$. Provided that no wavenumber resonance occurs (i.e. $2\alpha_1 \neq \alpha_2$ assuming that $\alpha_1 < \alpha_2$) the only extra terms which contribute to the right-hand side of equation (D.1) are those proportional to $E_1$. The additional equation, similar to equations (D.2)–(D.3), becomes

$$\left(B_{311}\mathsf{A}_{\alpha_1} - \frac{\partial B_{311}}{\partial t_0}\mathsf{B}\right)\boldsymbol{w}_{311} = \left[\mathrm{i}\frac{\partial B_1}{\partial y_1}\frac{\partial \mathsf{A}_{\alpha_1}}{\partial \alpha} + \left(\frac{\partial B_1}{\partial t_1} + \frac{\partial A_1}{\partial t_2}\right)\mathsf{B}\right]\boldsymbol{w}_{111} \quad \text{(E.4)}$$

The equation for $\varepsilon^3 E_2$, i.e. the second mode, is similar.

Following the steps developed in Appendix D and recollecting that $B_1 = B_1(Y_{12}, \ldots)$ we deduce that $B_{311} = \partial B_1/\partial Y_{12}$ and $\partial A_1/\partial t_2 = K_4 \partial B_1/\partial Y_{12}$, so that subsequently we have

$$\mathsf{L}_{\alpha_1,\sigma_1}\boldsymbol{w}_{311}^{(2)} = \left[\mathrm{i}\frac{\partial \mathsf{A}_{\alpha_1}}{\partial \alpha} + (K_4 - c_{g2})\mathsf{B}\right]\boldsymbol{w}_{111}\,. \quad \text{(E.5)}$$

The solvability condition applied to equation (E.5) results in

$$K_4 = c_{g2} - c_{g1},$$

so that the evolution equation for $A_1$ at third order becomes

$$\frac{\partial A_1}{\partial t_2} = K_{11}A_1|A_1|^2 + K_{12}A_1|A_2|^2 + K_2\frac{\partial^2 A_1}{\partial Y_{11}^2} - c_{g1}\frac{\partial A_1}{\partial y_2} + (c_{g2} - c_{g1})\frac{\partial B_1}{\partial Y_{12}}\,. \quad \text{(E.6)}$$

This equation is identical to equation (12) given by Knobloch and De Luca (1990) in the case of counter-propagating waves where $c_{g2} = -c_{g1}$. If $c_{g2} = c_{g1}$ then the last term in (E.6) disappears and the equation becomes the standard coupled CGLE. Although this equation is local in nature, it does not lead to any problem since in this case the two wave envelopes travel together

and interact (locally) indefinitely. When the group speeds are different, the uniform validity of (E.6) requires the solvability condition with respect to the modulational amplitude $B_1$ to be satisfied. It is obtained by integrating this equation with respect to $Y_{12}$ over the flow region and imposing homogeneous boundary conditions for $B_1$ at the ends. The resulting amplitude equation for slow time then becomes

$$\frac{\partial A_1}{\partial t_2} = K_{11} A_1 |A_1|^2 + K_{12} \lambda_1 A_1 + K_2 \frac{\partial^2 A_1}{\partial Y_{11}^2} - c_{g1} \frac{\partial A_1}{\partial y_2}\,, \tag{E.7}$$

where

$$\lambda_1 = \frac{1}{A_H} \int_{-c_{g2} t_1}^{A_H - c_{g2} t_1} |A_2|^2 \, \mathrm{d}Y_{12} \tag{E.8}$$

and $A_H$ is the dimensionless height of the enclosure. The derivation of the evolution equation for $A_2$ is identical. Finally, reconstituting the full amplitude equations for both $A_1$ and $A_2$ as done in Appendix D we obtain equations (26)–(28).

## References


Aranson, I., Kramer, L., 2002. The world of the complex Ginzburg-Landau equation. Rev. Mod. Phys. 79 (1), 99–143.

Bergholtz, R. F., 1978. Instability of steady natural convection in a vertical fluid layer. J. Fluid Mech. 84, 743–768.

Brevdo, L., 1988. A study of absolute and convective instabilities with an application to the Eady model. Geophys. Astrophys. Fluid Dyn. 40, 1–92.

Brevdo, L., 1995. Convectively unstable wave packets in the Blasius boundary layer. Z. Angew. Math. Mech. 6, 423–436.

Büchel, P., Lücke, M., 2000. Localized perturbations in binary fluid convection with and without throughflow. Phys. Rev. E 63, 016307.

Büchel, P., Lücke, M., Roth, D., Schmitz, R., 1996. Pattern selection in the absolutely unstable regime as a nonlinear eigenvalue problem:Taylor vortices in axial flow. Phys. Rev. E 53 (5), 4764–4777.

Carrière, P., Monkewitz, P., 1999. Convective versus absolute instability in mixed Rayleigh-Bénard-Poiseuille convection. J. Fluid Mech. 384, 243–262.

Chenoweth, D. R., Paolucci, S., 1985. Gas flow in vertical slots with large horizontal temperature differences. Phys. Fluids 28, 2365–2374.

Chenoweth, D. R., Paolucci, S., 1986. Natural convection in an enclosed vertical air layer with large horizontal temperature differences. J. Fluid Mech. 169, 173–210.

Chomaz, J.-M., 1992. Absolute and convective instabilities in nonlinear systems. Phys. Rev. Lett. 69 (13), 1931–1934.

Couairon, A., Chomaz, J.-M., 1997. Absolute and convective instabilities, front velocities and global modes in nonlinear systems. Physica D 108, 236–276.

Craik, A. D. D., 1985. Wave interactions and fluid flows. Cambridge University Press.

Cross, M. C., Hohenberg, P., 1993. Pattern formation outside of equilibrium. Rev. Mod. Phys. 65 (3), 853–1112.

Cross, M. C., Kuo, E., 1992. One dimensional spatial structure near a Hopf bifurcation at finite wavenumber. Physica D 59, 90–120.

Daniels, K., Plapp, B., Bodenschatz, E., 2000. Pattern formation in inclined layer convection. Phys. Rev. Lett. 84 (23), 5320–5323.

Dauchot, O., Manneville, P., 1997. Local versus global concepts in hydrodynamic stability theory. J. Phys. II France 7, 371–389.

Deissler, R. J., 1986. Spatially growing waves, intermittency, and convective chaos in an open-flow system. Physica D 25, 233–260.

Deissler, R. J., 1987. The convective nature of instability in plane Poiseuille flow. Phys. Fluids 30, 2303–2305.

Delbende, I., Chomaz, J.-M., 1998. Nonlinear convective/absolute instabilities in parallel two-dimensional wakes. Phys. Fluids 10 (11), 2724–2736.

Fineberg, J., Steinberg, V., 1997. Vortex-front propagation in railegh-bénard convection. Phys. Rev. Lett. 58, 1332.

Herbert, T., 1983. On perturbation methods in nonlinear stability theory. J. Fluid Mech. 126, 167–186.

Huerre, P., 2000. Perspectives in Fluid Dynamics. A collective Introduction to Current Research. Cambridge University Press, Ch. 4, Open Shear Flow Instabilities, pp. 159–229.

Huerre, P., Monkewitz, P. A., 1985. Absolute and convective instabilities in free shear layers. J. Fluid Mech. 159, 151–168.

Huerre, P., Monkewitz, P. A., 1990. Local and global instabilities in spatially developing flows. Ann. Rev Fluid Mech. 22, 473–537.

IMSL Inc., 1989. IMSL mathematical library, version 1.1. Tech. rep., Houston, TX.

Knobloch, E., De Luca, J., 1990. Amplitude equations for travelling wave convection. Nonlinearity 3, 975–980.

Landman, M., 1987. Solutions of the Ginzburg-Landau equation of interest in shear flow transition. Stud. Appl. Math. 76, 187–237.

Lee, Y., Korpela, S., 1983. Multicellular natural convection in a vertical slot. J. Fluid Mech. 126, 91–121.

Lingwood, R., 1997. On the application of the Briggs' and steepest-descent methods to a boundary layer flow. Stud. Appl. Math. 98, 213–254.

Moresco, P., Healey, J. J., 2000. Spatio-temporal mixed convection boundary layers. J. Fluid Mech. 402, 89–107.

Müller, H. W., Tveitereid, M., Trainoff, S., 1993. Rayleigh-Bénard prblem with imposed weak through-flow: Two coupled Ginzburg-Landau equations.

Phys. Rev. E 48, 263–272.
Newell, A. C., 1974. Envelope equations. Lectures in Appl. Math. 15, 157–163.
Nozaki, K., Bekki, N., 1983. Pattern selection and spatiotemporal transition to chaos in the Ginzburg-Landau equation. Phys. Rev. Lett. 51, 2171–2174.
Nozaki, K., Bekki, N., 1984. Exact solutions of the generalized Ginzburg-Landau equation. J. Phys. Soc. Japan 53, 1581–1582.
Paolucci, S., 1982. On the filtering of sound from the Navier-Stokes equations. Tech. Rep. SAND, Sandia National Laboratories, Livermore, California.
Pier, B., Huerre, P., 1996. Fully nonlinear global modes in spatially developing media. Physica D 99, 206–222.
Pierce, R., Wayne, C., 1995. On the validity of mean-field amplitude equations for counterpropagating wavetrains. Nonlinearity 8, 769–779.
Priede, J., Gerberth, G., 1997. Convective, absolute, and global instabilities of thermocapillary-buoyancy convection in extended layers. Phys. Rev. E 56 (4), 4187–4199.
Reynolds, W. C., Potter, M. C., 1967. Finite-amplitude instability of parallel shear flows. J. Fluid Mech. 27, 465–492.
Rudakov, R. N., 1967. Spectrum of perturbations and stability of convective motion between vertical plates. Appl. Math. Mech. 31, 376–383.
Sen, P., Venkateswarlu, D., 1983. On the stability of plane Poiseuille flow to finite-amplitude disturbances, considering higher-order Landau coefficients. J. Fluid Mech. 133, 179–206.
Simpkins, P., 1989. Transition to periodic convective states in an air filled slot. Bull. Am. Phys. Soc. 34, 2271.
Simpkins, P., 1993. Personal communications.
Stuart, J. T., 1960. On the non-linear mechanics of wave disturbances in stable and unstable parallel flows. Part 1. The basic behaviour in plane Poiseuille flow. J. Fluid Mech 9, 353–370.
Stuart, J. T., Stewartson, K., 1971. A non-linear instability theory for a wave system in plane Poiseuille flow. J. Fluid Mech. 48, 529–545.
Suslov, S. A., 1997. Nonlinear analysis of non-Boussinesq convection. Ph.D. thesis, University of Notre Dame, USA.
Suslov, S. A., Paolucci, S., 1995a. Stability of mixed-convection flow in a tall vertical channel under non-Boussinesq conditions. J. Fluid Mech. 302, 91–115.
Suslov, S. A., Paolucci, S., 1995b. Stability of natural convection flow in a tall vertical enclosure under non-Boussinesq conditions. Int. J. Heat Mass Transfer 38, 2143–2157.
Suslov, S. A., Paolucci, S., 1997a. Non-Boussinesq convection in a tall cavity near the codimension-2 point. In: Ulucakli et al., M. E. (Ed.), Proceedings of the ASME Heat Transfer Division. Vol. 3, HTD-353. ASME Press, pp. 243–250.
Suslov, S. A., Paolucci, S., 1997b. Nonlinear analysis of convection flow in a tall vertical enclosure under non-Boussinesq conditions. J. Fluid Mech. 344, 1–41.

Suslov, S. A., Paolucci, S., 1999. Nonlinear stability of mixed convection flow under non-Boussinesq conditions. Part 2. Mean flow characteristics. J. Fluid Mech. 398, 87–108.

Tobias, S., Proctor, M., Knobloch, E., 1998. Convective and absolute instabilities of fluid flows in finite geometry. Physica D 113, 43–72.

Watson, J., 1960. On the non-linear mechanics of wave disturbances in stable and unstable parallel flows. Part 2. The development of a solution for plane Poiseuille flow and for plane Couette flow. J. Fluid Mech. 9, 371–389.

White, F. M., 1974. Viscous Fluid Flow. McGraw-Hill.